J. Fluid Mech. (2000), *vol.* 413, *pp.* 1–47. Printed in the United Kingdom

© 2000 Cambridge University Press

The anatomy of the mixing transition in homogeneous and stratified free shear layers

By C. P. CAULFIELD[1]† AND W. R. PELTIER[2]

[1]Centre for Environmental and Geophysical Flows, School of Mathematics, University of Bristol, University Walk, Bristol BS8 1TW, UK

[2]Department of Physics, University of Toronto, Toronto, Ontario, M5S 1A7, Canada

(Received 8 May 1998 and in revised form 6 January 2000)

We investigate the detailed nature of the 'mixing transition' through which turbulence may develop in both homogeneous and stratified free shear layers. Our focus is upon the fundamental role in transition, and in particular the associated 'mixing' (i.e. small-scale motions which lead to an irreversible increase in the total potential energy of the flow) that is played by streamwise vortex streaks, which develop once the primary and typically two-dimensional Kelvin–Helmholtz (KH) billow saturates at finite amplitude.

Saturated KH billows are susceptible to a family of three-dimensional secondary instabilities. In homogeneous fluid, secondary stability analyses predict that the streamwise vortex streaks originate through a 'hyperbolic' instability that is localized in the vorticity braids that develop between billow cores. In sufficiently strongly stratified fluid, the secondary instability mechanism is fundamentally different, and is associated with convective destabilization of the statically unstable sublayers that are created as the KH billows roll up.

We test the validity of these theoretical predictions by performing a sequence of three-dimensional direct numerical simulations of shear layer evolution, with the flow Reynolds number (defined on the basis of shear layer half-depth and half the velocity difference) $Re = 750$, the Prandtl number of the fluid $Pr = 1$, and the minimum gradient Richardson number $Ri(0)$ varying between 0 and 0.1. These simulations quantitatively verify the predictions of our stability analysis, both as to the spanwise wavelength and the spatial localization of the streamwise vortex streaks. We track the nonlinear amplification of these secondary coherent structures, and investigate the nature of the process which actually triggers mixing. Both in stratified and unstratified shear layers, the subsequent nonlinear amplification of the initially localized streamwise vortex streaks is driven by the vertical shear in the evolving mean flow. The two-dimensional flow associated with the primary KH billow plays an essentially catalytic role. Vortex stretching causes the streamwise vortices to extend beyond their initially localized regions, and leads eventually to a streamwise-aligned collision between the streamwise vortices that are initially associated with adjacent cores.

It is through this collision of neighbouring streamwise vortex streaks that a final and violent finite-amplitude subcritical transition occurs in both stratified and unstratified shear layers, which drives the mixing process. In a stratified flow with appropriate initial characteristics, the irreversible small-scale mixing of the density which is triggered by this transition leads to the development of a third layer within

† Present address: Department of Mechanical and Aerospace Engineering, University of California, San Diego, 9500 Gilman Drive, La Jolla, CA 92093-0411, USA.

the flow of relatively well-mixed fluid that is of an intermediate density, bounded by narrow regions of strong density gradient.

1. Introduction

The spontaneous development of spatially incoherent turbulent motion within an initially laminar fluid flow is a problem of fundamental importance in fluid dynamics (see e.g. Bayly, Orszag & Herbert 1988) with applications in both the geophysical sciences (see the reviews of Thorpe 1987 and Fernando 1991) and engineering (e.g. Hussain 1983). Flows with a point of inflection in the initially laminar velocity profile are known to be primarily unstable to a two-dimensional instability that is often referred to as the 'Kelvin–Helmholtz', or KH instability (see Drazin & Reid 1981 for a thorough introduction). In this paper, we will consider the life cycle of four particular examples of such flows, both with and without density variations, as they undergo the transition to turbulence, by which we mean to imply a state characterized by the proliferation of small-scale, uncorrelated motions.

As the KH instability develops to finite amplitude, the unstratified or homogeneous mixing layer, which may be considered to constitute a strip of vorticity, rolls up into an array of two-dimensional elliptical vortices, or 'billows'. Brown & Roshko (1974) experimentally verified the expected initial behaviour involving the largely two-dimensional growth of coherent spanwise vortical structures separated by a braid region of high strain. Though this circumstance is generic, experiments have also revealed dislocations or significant spanwise variation in the primary spanwise vortices that develop in wide channels (Browand & Prost-Domasky 1990; Nygaard & Glezer 1990, 1991, 1994; Atsavapranee & Gharib 1997).

The primary KH vortices are not totally isolated from each other, but rather are connected by a thin 'braid' of spanwise vorticity, as discussed by Corcos & Sherman (1984). This thin braid of vorticity is a remnant of the initial spanwise vorticity of the shear layer, and is embedded in a region of flow with open streamlines that are locally hyperbolic, such that a stagnation point exists at the midpoint of the braid. A typical distribution of spanwise vorticity for a fully-developed KH billow in an unstratified flow is shown in figure 1(*a*).

When largely two-dimensional arrays of primary spanwise vortices develop in mixing layers, the vortices themselves are known to be subject in turn to a wide variety of secondary instabilities, both quasi-two-dimensional and inherently three-dimensional in nature. Perhaps the most well-known of these is the subharmonic pairing instability (see Winant & Browand 1974) in which pairs of the primary KH vortices precess around each other and eventually merge to form a larger vortex. However, experimental evidence from both unstratified and stratified shear layers strongly suggests that the spontaneous appearance of initially coherent small-scale three-dimensional motions is an essential precursor to the transition to fully-developed disordered turbulent flow. In this paper we therefore intend to focus upon the origins of three-dimensional structure within an initially two-dimensional KH billow so that we may consider the processes of small-scale three-dimensionalization in isolation.

In unstratified shear layers, experiments have shown that it is the vorticity braids that become the site of strong three-dimensional motions, that initially take the form of streamwise vortex streaks, often referred to as rib vortices (see Hussain 1983 for a review). These coherent rib vortices are precursory to the appearance of small-scale

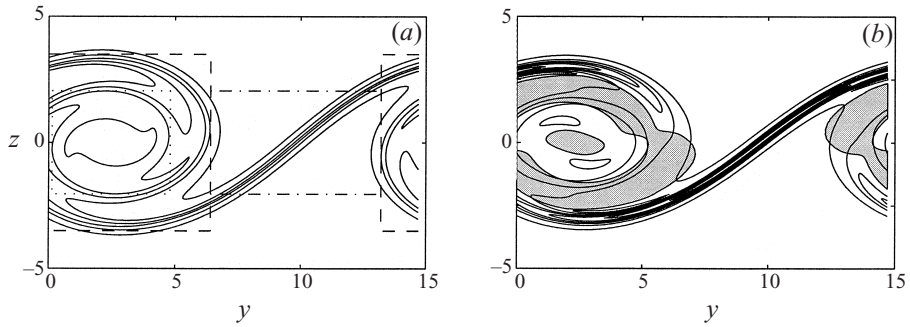

FIGURE 1. (*a*) Contours of spanwise vorticity in a fully-developed KH billow in an unstratified shear flow, at a time when the perturbation has maximum amplitude. Compartmentalization of the flow into core (dotted rectangle), eyelid (dashed rectangle) and braid regions (dot-dashed rectangle) is also shown. (*b*) Contours of spanwise vorticity in a fully-developed KH billow in a flow with $Ri(0) = 0.05$, at a time when the perturbation has maximum amplitude. Shading denotes regions of static instability. The Reynolds number $Re = 750 = Ud/\nu$, where U and d are half the velocity difference and the shear half-depth respectively, and the Prandtl number $Pr = \nu/k = 1$ where ν is the kinematic viscosity and κ is the thermal diffusivity.

disordered motion and the transition to turbulence in homogeneous free shear layers, and have been much studied both numerically and experimentally (see for example Corcos & Lin 1984; Lin & Corcos 1984; Bernal & Roshko 1986; Metcalfe *et al.* 1987; Lasheras, Cho & Maxworthy 1986; Lasheras & Choi 1988; Ashurst & Meiburg 1988; Klaassen & Peltier 1989, 1991; Nygaard & Glezer 1991; Rogers & Moser 1992; Knio & Ghoniem 1992; Smyth & Peltier 1994; Schowalter, Van Atta & Lasheras 1994; Lesieur, Comte & Métais 1995; Potylitsin & Peltier 1998).

It is well-known that both the elliptical KH vortex core (see Pierrehumbert & Widnall 1982; Cambon, Teissèdre & Jeandal 1985; Bayly 1986; Pierrehumbert 1986; Landman & Saffman 1987; Klaassen & Peltier 1989; Waleffe 1990; Nygaard & Glezer 1990, 1991; Smyth & Peltier 1994; Salhi, Cambon & Speziale 1997; Potylitsin & Peltier 1998) and the hyperbolic braid region (Klaassen & Peltier 1991, henceforth KP91; Smyth & Peltier 1994) are subject to distinct, fundamentally three-dimensional secondary instabilities. Smyth & Peltier (1994) showed that the braid-centred 'hyperbolic' instability is predicted to have larger growth rate than the core-centred 'elliptic' instability provided the spanwise wavelength of the perturbation is sufficiently small. One of the principal objectives of this paper is to clarify the initial growth mechanism of the principal secondary instability of a homogeneous shear layer. We demonstrate unequivocally that the development of three-dimensional motions in a primary KH billow is dominated by the onset of a braid-centred hyperbolic instability, which is fundamentally distinct from the 'elliptical' instability.

To distinguish between the braid-centred and core-centred instabilities, we consider the spatial localization of the three-dimensional perturbations in detail. We find that it is helpful to compartmentalize all perturbation quantities (in particular, appropriately defined perturbation kinetic energies) into different bins, associated with the primary billow core, the billow periphery (or 'eyelid') and the braid region, as shown in figure 1(*a*). For simplicity, we have chosen these bins to be rectangular, and defined them in terms of the spanwise vorticity contours of a two-dimensional, unstratified shear layer. The 'core' region was defined as the minimal rectangle containing fluid with spanwise vorticity that is at least 70% of the maximum value within the flow. The vertical extent of this region also defines the vertical extent of the 'braid' region. The

'eyelid' region (of particular relevance in stratified flows) is defined as the rectangular region which surrounds the 30% contour of spanwise vorticity. The braid region is also rectangular, extending horizontally between the two edges of the eyelid region.

The natural question arises as to precisely how such three-dimensional structures extract energy from the two-dimensional flow. Analogously with studies of boundary-layer flows (Orszag & Patera 1983; Herbert 1988) we find that three-dimensional motions in a mixing layer appear to grow initially by extracting energy directly from the horizontally averaged mean flow. Although the presence of a two-dimensional perturbation (i.e. the KH billow) is essential to the growth of the three-dimensional perturbation, it largely plays a catalytic role (in the sense of there being little energy transfer from the two-dimensional perturbation into the three-dimensional perturbation) at least initially.

Having addressed the issues of initial development and subsequent growth of three-dimensional perturbations of an unstratified shear layer, we will also seek to understand how the actual transition to turbulence occurs within the free shear layer. Ruelle & Takens (1971) conjectured on topological grounds that the generic pathway to turbulence for a fluid flow is through the sequential onset of a finite (and small) number of instabilities, an ansatz which is consistent with the experimental evidence for a broad range of flows (see Swinney & Gollub 1981 for a review). Such a pathway is particularly appealing for the unstratified mixing layer, especially if subharmonic merging events or 'pairing' is delayed, or at least does not initiate immediately. Then, the initially laminar flow is subject to the KH billow instability, which in turn is subject to a secondary (three-dimensional) instability in the form of streamwise vortices. Whether these vortices are themselves subject to a tertiary instability, or lead directly to turbulent disordered motion within the flow is an important open question which we also address in this paper.

It is well-known that the KH instability may occur in flows with statically stable density distributions, provided the Richardson number Ri is less than $\frac{1}{4}$ somewhere within the flow (a result established for inviscid flows by Miles 1961 and Howard 1961) in which Ri is defined as

$$Ri(z) = \frac{-g}{\rho}\frac{\partial \rho}{\partial z}\Big/\left(\frac{\mathrm{d}\bar{V}}{\mathrm{d}z}\right)^2, \tag{1.1}$$

where $\rho(z)$ and $\bar{V}(z)$ are the background profiles of density and velocity respectively. In figure 1(b), we show vorticity contours of a KH billow within a stratified shear layer with initial midplane Richardson number equal to 0.05.

In his classic tilted tank experiments, Thorpe (1985, 1987) observed that stratified mixing layers were also subject to a rolling up of the spanwise vorticity into distinct KH billows. These vortices were in turn subject to a wide variety of secondary instabilities. Subharmonic merging was still observed to occur in a largely two-dimensional manner, although compared to unstratified shear flows, there is evidence that the stratification suppresses merging somewhat (see Koop & Browand 1979; Schowalter *et al.* 1994). Streamwise periodic structures were also observed, both in the braid region (referred to as 'tubes' by Thorpe) and also around the periphery of the KH billow cores, with an observed variation in their characteristic periodicity with Re. Similar structures were also reported, and identified as vortices by Lawrence, Browand & Redekopp (1991) and Schowalter *et al.* (1994).

Peltier, Hallé & Clark (1978) and Davis & Peltier (1979) have conjectured the existence of an alternative process of three-dimensionalization in a stratified shear

flow to that which governs the process in homogeneous fluid. During the process of rolling up, a KH instability in a stratified flow advects the density field in such a way as to induce convectively unstable layering of the density field in the regions surrounding the vortex core (shown as shaded regions in figure 1*b*). A necessary condition (Gallagher & Mercer 1965; Kelly 1967; Domaradzki & Metcalfe 1988; Clever & Busse 1991) for such statically unstable regions to actually be unstable to a convective-type instability is that the convection rolls be aligned with the direction of the background shear, i.e. that the rolls have streamwise aligned vorticity within the present context. Therefore, provided these statically unstable layers are sufficiently deep, so that their associated Rayleigh number is sufficiently high (as specifically discussed by Davis & Peltier 1979) streamwise vortical overturnings are expected which scale with the depth of the deepest statically unstable layer (which is naturally the one on the periphery of the primary billow core, in the 'eyelid' region shown in figure 1). Klaassen & Peltier (1985*a*) (henceforth KP85) and KP91 considered the secondary stability of such flows in detail at similar Reynolds numbers to those attained by Thorpe in his experiments.

At finite amplitude, these overturnings develop into periodic arrays of streamwise vortex tubes of alternating sign, with maximum amplitude around the periphery of the vortex core. The characteristic spanwise wavelength of these convectively induced streamwise vortices is significantly smaller than the streamwise wavelength of the primary KH billows, and is slightly less than, though of the same order as, the spanwise wavelength of the most unstable unstratified hyperbolic instability mode predicted by secondary stability analysis. In our previously reported simulation (Caulfield & Peltier 1994, see also Palmer, Fritts & Andreassen 1996; Cortesi, Yadigaroglau & Bannerjee 1998), we observed that the dominant spanwise wavelength of the numerically generated streamwise vortices agreed very well with the most unstable mode determined from a stability analysis using the method of KP85 and KP91. For the particular value of Re selected, transition to highly disordered motion occurred rapidly after the onset of the secondary convective instability. Furthermore, the appearance of streamwise vortices appeared to suppress the subharmonic pairing instability.

In the context of our analyses of a stratified shear flow, we wish to identify the primary mechanisms by which the flow becomes three-dimensionally unstable, and the spatial region within which perturbations grow. In particular, we wish to determine if the statically unstable regions around the periphery of the primary vortex core are fundamental to the development of three-dimensional motions, as predicted theoretically. We will also consider the way in which these motions evolve and interact dynamically with the ambient stratification.

In § 2, we briefly discuss the characteristics of the numerical model and the various energy budgets which we use in our analysis. In this section we describe the algorithm (essentially that due to Winters *et al.* 1995) which we use to decompose the potential energy $\mathscr{P}$ into two constituent parts, namely the 'available' potential energy $\mathscr{P}_A$ and the 'background' (or minimum) potential energy $\mathscr{P}_B$. In a dissipative flow at finite Reynolds number, $\mathscr{P}_B$ can increase due to mixing or diffusion (an irreversible conversion from the internal energy of the fluid) while $\mathscr{P}_A = \mathscr{P} - \mathscr{P}_B$ is 'available' to be converted into kinetic energy for motion.

In § 3, we describe the results obtained in a series of two-dimensional simulations of stratified shear layers for four different values of the initial midplane Richardson number $Ri(0)$. Only through a detailed understanding of such two-dimensional flows are we able to quantify the crucial effect of three-dimensionality on flow evolution.

In § 4, we present the results of a secondary stability analysis (using the technique developed in KP85 and KP91) and summarize the properties of the three-dimensional instabilities which are possible candidates for control of the mixing transition, i.e. the onset of significantly enhanced irreversible mixing due to small-scale disordered motions.

Section 5 is devoted to a detailed discussion of the bulk characteristics of three-dimensional simulations of stratified shear layers, with the same initial profiles as employed in the two-dimensional analyses discussed in § 3. In particular, on the basis of perturbation kinetic energy and available potential energy considerations, we identify the dominant mechanisms of initial growth of three-dimensional motions and compare the results with the theoretical predictions presented in § 4. Through a careful analysis of flow energetics, we find that, over a range of Richardson numbers, the density field plays a largely catalytic role in the finite-amplitude development of three-dimensional perturbations. Perturbations in the density field trigger the onset of three-dimensional motions, and determine the nucleation sites of streamwise vortices, away from the braid region and around the periphery of the primary vortex core. However, the primary mechanism for enhancement of the three-dimensional motions is through shear extraction directly from the mean, background flow.

Our results demonstrate that there is also a close correspondence between the unstratified and stratified flows in the final transition to disordered motion, this transition being due to a subcritical finite-amplitude interaction between streamwise vortices colliding in the braid region into which they have been stretched and advected by the strain field induced by the mean flow in both cases. This final stage of the transition is the one which initiates mixing and in the case of stratified flow we observe an associated increase in the background potential energy of the system $\mathscr{P}_B$. We use an appropriate representation of the mixing efficiency of a three-dimensional stratified shear layer, i.e. the ratio of the (irreversible) increase of the potential energy of the system to the work done on the fluid, which is closely related to that used in shear-free experiments (see Linden 1979 and Fernando 1991 for reviews, and Park, Whitehead & Gnanadeskian 1994). From our analyses we are able to infer that the mixing induced by the breakdown of KH instabilities should lead naturally to the development of a layered density profile, once the disordered motion has decayed.

In § 6, we present appropriate visualizations of the three-dimensional flow fields and thus identify the spatial structure of the varying physical processes by which the flows become disordered and finally mixed as $Ri(0)$ changes. We provide a summary of our conclusions in § 7.

2. Mathematical model

We consider a temporal shear layer, i.e. a flow which is statistically uniform in space, and which evolves with time. We restrict our attention to incompressible flows in which the density variations are sufficiently small so that the Boussinesq approximation is valid. The initial background profiles of velocity and density will be assumed to be, respectively,

$$\bar{V}(z,0) = V_0 \tanh \frac{z}{d}, \tag{2.1}$$

$$\bar{\rho}(z,0) = \rho_a - \rho_0 \tanh \frac{Rz}{d}, \tag{2.2}$$

in which R is the ratio of the characteristic scale of velocity variation to the characteristic scale of density variation. This choice of initial conditions, together with the

coordinate system that we use (i.e. the x-coordinate axis is in the spanwise or cross-stream direction, the y-coordinate axis is in the streamwise or along-stream direction and the z-coordinate axis is in the vertical direction) means that the shear layer constitutes a layer of *negative* spanwise vorticity. In these calculations, we chose the experimentally realistic value of $R = 1.1$ (see Thorpe 1985, 1987; Caulfield, Yoshida & Peltier 1996). For such a value of R, we know that the flow is primarily unstable to the KH instability (see Smyth, Klaassen & Peltier 1988 for a full discussion). For the profiles chosen, the initial Richardson number is a minimum at the midpoint of the shear layer (i.e. at $z = 0$) with value

$$Ri(0) \equiv \frac{gR\rho_0 d}{\rho_a V_0^2} \equiv RRi_0, \tag{2.3}$$

where Ri_0 is the bulk Richardson number of the flow. Throughout this paper, we will use $Ri(0)$ as an appropriate measure of the importance of stratification within the flow.

Using V_0, ρ_0 and d as characteristic velocity variation, density variation and length scales, the governing equations of motion are

$$\frac{\mathrm{D}u_i^*}{\mathrm{D}t^*} = -\frac{\partial p'^*}{\partial x_i^*} - \frac{Ri(0)}{R}\rho'^*\delta_{i3} + \frac{1}{Re}\frac{\partial^2 u_i^*}{\partial x_j^{*2}}, \tag{2.4}$$

$$\frac{\partial u_j^*}{\partial x_j^*} = 0, \tag{2.5}$$

$$\frac{\mathrm{D}\rho^*}{\mathrm{D}t^*} = \frac{1}{RePr}\frac{\partial^2 \rho^*}{\partial x_j^{*2}}, \tag{2.6}$$

in which asterisks denote non-dimensional quantities, primes denote departure from hydrostatic balance, summation is implied by repeated subscripts, and $\mathrm{D}/\mathrm{D}t$ represents the material derivative. Henceforth, we will only consider non-dimensional quantities, and so we will drop the asterisks. Also, we drop the primes on p and ρ.

Characteristics of the flow depend on three non-dimensional parameters: the Reynolds number Re, the Prandtl number Pr and the midplane Richardson number $Ri(0)$. For simplicity, we have chosen the Prandtl number $Pr \equiv \nu/\kappa = 1$ in all simulations. This value is of the same order as typical atmospheric values (e.g. in air $Pr \sim 0.7$) but is appreciably smaller than typical experimental values (in which $Pr \sim 700$, if salt-stratified water is the experimental fluid). Therefore, it is important to remember that mass diffuses appreciably more rapidly relative to momentum in our simulations than would be the case in a salt-stratified fluid. We chose the Reynolds number to be 750 (a typical experimental value) where $Re = V_0 d/\nu$. Finally, and in order to investigate the effect of weak to moderate density stratification, we have chosen to analyse flows with the four values of $Ri(0) = RRi_0 = 0$, 0.025, 0.05 and 0.1.

All of our numerical simulations of the process of turbulent collapse of stratified mixing layers were conducted using a modified version of an anelastic model (see Clark 1977 and Peltier *et al.* 1978 for further details). This model is based upon the use of second-order accurate finite differences to solve (2.4)–(2.6) on a staggered grid, while the equations are stepped forward in time using an explicit leapfrog scheme, which is stabilized by the introduction of an Euler backwards step every 10 time steps. The streamwise extent L_y of the computational domain was taken in all cases to be equal to one wavelength λ of the most unstable mode of linear inviscid theory

(see Drazin & Reid 1981) for the background profiles defined by (2.1) and (2.2). This implies $L_y \simeq 14.7d$.

The spanwise extent L_x was chosen to be 10 shear half-depths, i.e. $L_x = 10d$. This extent was chosen to be sufficiently wide so that core-centred modes (with wavelengths of the order of (0.6–0.7) λ, as discussed by Nygaard & Glezer 1990, 1991) would be allowed to grow within the flow domain. This spanwise extent also allows the development of multiple streamwise vortices in the spanwise direction, and so will provide a basis on which to compare the theoretically predicted spanwise scale with that delivered by the numerical simulations.

Periodicity in both the spanwise and the streamwise direction was imposed upon the numerical simulations. Our computations for the most part consider the development of a single KH billow, and exclude the possibility of subharmonic instabilities. We impose free-slip and no-normal-flow boundary conditions for the velocity components at the vertical boundaries of the domain, as well as no stress, and zero density flux. The vertical extent (for comparison with the multiple billow calculations briefly reported in Caulfield & Peltier 1994) was set at 20 shear layer half-depths, i.e. $-10 < z < 10$. Through various resolution checks, we found that we were obliged to include 100 gridpoints in each coordinate direction (i.e. $N_x = N_y = N_z = 100$). This seemed to be sufficient for proper description of the three-dimensional motion. For direct comparison, we used the same streamwise and vertical grid, and identical non-dimensional parameters for the two-dimensional calculations.

To investigate the development of such flows with time, we decompose the various flow fields into mean and perturbation parts. Furthermore, since we believe that the development of three-dimensional motions is crucial to the behaviour of the flow, we wish to further subdivide the perturbation velocity field into a spanwise averaged part, and an inherently three-dimensional deviation.

To conduct our analyses at any particular instant in time, we therefore consider the total three-dimensional flow field which has developed from initial conditions defined by (2.1)–(2.2), and write the velocity fields as

$$\boldsymbol{u}(x,y,z,t) = [u(x,y,z,t), v(x,y,z,t), w(x,y,z,t)], \tag{2.7}$$

$$\bar{\boldsymbol{V}}(z,t) = \langle \boldsymbol{u} \rangle_{xy} = [0, \bar{V}(z,t), 0], \tag{2.8}$$

$$\boldsymbol{u}_{kh}(y,z,t) = \langle \boldsymbol{u} - \bar{\boldsymbol{V}} \rangle_x = [0, v_{kh}, w_{kh}], \tag{2.9}$$

$$\boldsymbol{u}_{3d}(x,y,z,t) = \boldsymbol{u} - \boldsymbol{u}_{kh} - \bar{\boldsymbol{V}} = \boldsymbol{u} - \langle \boldsymbol{u} \rangle_z = [u_{3d}, v_{3d}, w_{3d}], \tag{2.10}$$

where the subscript kh refers to the spanwise-averaged perturbation, which we identify with the primary KH billow, and the subscript $3d$ refers to the perturbation which deviates from spanwise-averaged flow. In these expressions $\langle . \rangle_p$ denotes an average in the p-direction, i.e.

$$\langle f(x,y,z) \rangle_p \equiv \frac{1}{L_p} \int_0^{L_p} f(x,y,z)\, \mathrm{d}p, \tag{2.11}$$

where p is either x, y or z.

It is possible to decompose the density field in a similar way, to obtain

$$\bar{\rho}(z,t) = \langle \rho \rangle_{xy}, \tag{2.12}$$

$$\rho_{kh}(y,z,t) = \langle \rho - \bar{\rho} \rangle_x, \tag{2.13}$$

$$\rho_{3d}(x,y,z,t) = \rho - \langle \rho \rangle_x = \rho - \rho_{kh} - \bar{\rho}. \tag{2.14}$$

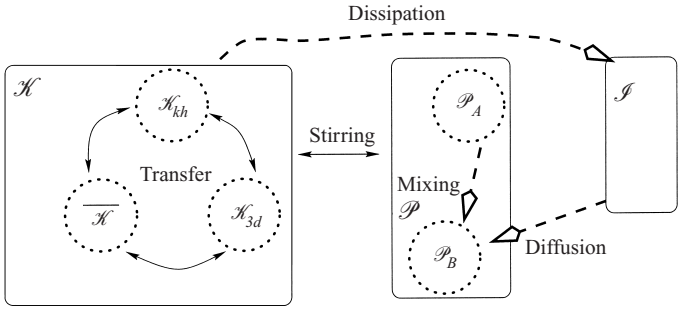

FIGURE 2. Schematic diagram of the total energy budget of the flow, showing all possible reversible changes (shown by solid lines and arrows) and irreversible changes (shown by dashed lines and hollow arrows) and exchanges between the kinetic energy $\mathscr{K}$, potential energy $\mathscr{P}$, and internal energy $\mathscr{I}$ of the flow.

To understand the evolution and development of perturbations within the flows under consideration, it is important to understand how energy may be redistributed as the perturbations evolve. The energy budget is shown schematically in figure 2 (following Winters *et al.* 1995) with the various possible energy conversions indicated.

2.1. *Kinetic energy*

In the Boussinesq approximation, we may identify the average total kinetic energy per unit mass of the flow over the computational domain as

$$\mathscr{K}(t) = \langle[(u^2 + v^2 + w^2)/2]\rangle_{xyz}, \tag{2.15}$$

which can be subdivided into three constituent parts analogously to the velocity and density fields as

$$\mathscr{K} = \bar{\mathscr{K}} + \mathscr{K}_{kh} + \mathscr{K}_{3d}, \tag{2.16}$$

where

$$\bar{\mathscr{K}} = \langle(\bar{V}^2)/2\rangle_z, \tag{2.17}$$

$$\mathscr{K}_{kh} = \langle(v_{kh}^2 + w_{kh}^2)/2\rangle_{yz}, \tag{2.18}$$

$$\mathscr{K}_{3d} = \langle(u_{3d}^2 + v_{3d}^2 + w_{3d}^2)/2\rangle_{xyz}. \tag{2.19}$$

These three average kinetic energies may be identified respectively as the average kinetic energy of the mean, background flow, the average kinetic energy associated with the spanwise-averaged two-dimensional perturbation, and the average kinetic energy of the three-dimensional deviation from the spanwise average. We average over the volume to remove dependence on the chosen volume of the domain.

The evolution equation for $\mathscr{K}(t)$ can be shown to be

$$\sigma = \frac{1}{2\mathscr{K}}\frac{\mathrm{d}}{\mathrm{d}t}\mathscr{K} = \frac{1}{2\mathscr{K}}\left(-\frac{Ri(0)}{R}\langle\rho w\rangle_{xyz} - \frac{1}{Re}\langle(\nabla\boldsymbol{u})^2\rangle_{xyz}\right), \tag{2.20}$$

$$\equiv \mathscr{H} + \mathscr{D}, \tag{2.21}$$

defining σ, a 'growth rate' for the total velocity $\boldsymbol{u}$. Instantaneously, $\langle|\boldsymbol{u}|\rangle_{xyz} \propto \exp(\sigma t)$ in general. Naturally, $\mathscr{D}$ is negative definite, and quantifies the loss of average kinetic energy (to the internal energy of the fluid) due to viscous dissipation. This loss is irreversible. The first term on the right-hand side of (2.20) is the (non-dimensional) buoyancy flux, which quantifies the exchange between the average total kinetic energy

of the flow and the average total potential energy of the flow. If $\mathscr{H}$ is positive, the net effect of the perturbations is to move relatively dense fluid downwards (and relatively light fluid upwards) thus reducing the total potential energy of the system, and thus increasing the total kinetic energy of the system. As an aside, the total kinetic energy budget equation may be employed as a very useful independent check on the accuracy of the numerical model, and for the resolution which we have chosen, this equation was satisfied to very high accuracy. Indeed, we found that the dominant source of error in (2.20) was due to the Boussinesq approximation, with the exact full kinetic energy equation for our flow being correct to within at most one part in 10^6, even when there was significant small-scale motion occurring.

We are principally interested in the development of three-dimensional motions, and so concentrate on the development of an evolution equation for $\mathscr{K}_{3d}$. As we shall see, three-dimensional motions are most significant when the KH billow has saturated, and so we are interested in the initial development of three-dimensional motions when

$$\mathscr{K}_{3d} \ll \bar{\mathscr{K}} + \mathscr{K}_{kh}. \tag{2.22}$$

Linearizing about the spanwise-averaged flow, we can estimate σ_{3d}, the instantaneous growth rate of the three-dimensional perturbation velocity (instantaneously $\langle |\boldsymbol{u}_{3d}| \rangle_{xyz} \propto \exp(\sigma_{3d} t)$ in general), from the equation

$$\begin{aligned}\sigma_{3d} = \frac{1}{2\mathscr{K}_{3d}} \frac{\mathrm{d}}{\mathrm{d}t} \mathscr{K}_{3d} = \frac{1}{2\mathscr{K}_{3d}} \Bigg[& - \left\langle v_{3d} w_{3d} \frac{\partial \bar{V}}{\partial z} \right\rangle_{xyz} - \left\langle \left(v_{3d}^2 \frac{\partial v_{kh}}{\partial y} + w_{3d}^2 \frac{\partial w_{kh}}{\partial z} \right) \right\rangle_{xyz} \\ & - \frac{1}{2} \left\langle \left(v_{3d}^2 - w_{3d}^2 \right) \left(\frac{\partial v_{kh}}{\partial y} - \frac{\partial w_{kh}}{\partial z} \right) \right\rangle_{xyz} \\ & - Ri_0 \langle \rho_{3d} w_{3d} \rangle_{xyz} - \frac{1}{Re} \left\langle (\boldsymbol{\nabla} \boldsymbol{u}_{3d})^2 \right\rangle_{xyz} \Bigg],\end{aligned} \tag{2.23}$$

$$\equiv \mathscr{S}\mathscr{H}\mathscr{B}_{3d} + \mathscr{S}\mathscr{H}\mathscr{K}\mathscr{H}_{3d} + \mathscr{S}\mathscr{T}_{3d} + \mathscr{H}_{3d} + \mathscr{D}_{3d}. \tag{2.24}$$

The dissipation term $\mathscr{D}_{3d}$ is negative definite. The three-dimensional perturbation kinetic energy can extract energy from both the mean background field (through $\mathscr{S}\mathscr{H}\mathscr{B}_{3d}$) and the two-dimensional KH flow field (through $\mathscr{S}\mathscr{H}\mathscr{K}\mathscr{H}_{3d}$) through the action of shearing, or tilting stresses.

Furthermore, the three-dimensional perturbation can also be subject to a stretching deformation through $\mathscr{S}\mathscr{T}_{3d}$ provided there is significant anisotropy in the three-dimensional perturbation field. By separating the two-dimensional fields into a horizontally averaged part, and a two-dimensional deviation from this horizontal average, we can investigate for any given perturbation whether contributions from the background flow or from the two-dimensional perturbation dominate the growth of the three-dimensional perturbation.

2.2. *Potential energy*

The exchange between the total kinetic energy of the system and the potential energy of the system is fundamental to the evolution of perturbations within stably stratified shear layers. It also parameterizes the amount of mixing within the flow. A reasonable working measure of the amount of mixing within a flow is the extent to which the total potential energy of the system increases. It is important to distinguish between reversible changes (stirring) and irreversible changes (mixing). Stirring must

be associated with larger scale motions within the flow, while mixing involves motions extending to the smallest scales.

If a parcel of relatively dense fluid is lifted upwards by the fluid motion, the total potential energy of the system is increased. However, if it is possible to return this parcel (without any change of its constituent parts) adiabatically to its original location, then the potential energy will return to its original value. The stirred fluid has, transiently, increased its potential energy by some amount, but this excess potential energy is still available to be converted back into kinetic energy. This concept of available potential energy or APE for exchange into kinetic energy of the flow, originally developed by Lorenz (1955), has had wide application in atmospheric dynamics. Winters *et al.* (1995) further developed the concept of a subdivision of average total potential energy $\mathscr{P}$ within stratified, dissipative flows into two parts: the background potential energy $\mathscr{P}_B$, which cannot be converted into kinetic energy, and the available potential energy $\mathscr{P}_A$, which can be so converted.

At any instant, the minimum, or background, average potential energy $\mathscr{P}_B$ of a fluid flow is the average potential energy associated with an adiabatic rearrangement of fluid parcels such that the variation of fluid density with height is strictly monotonic (and decreasing upwards) throughout the fluid. This rearrangement defines a notional, one-dimensional and strictly statically stable density distribution $\rho_B(z)$. Such a rearrangement is shown schematically in figure 3. It is assumed that the fluid may be subdivided into indivisible parcels, each of which has a constant density. These parcels are sufficiently small so that any motions of a smaller scale than a particular parcel must lead inevitably to an irreversible change in the constituents of that parcel. (In a finite difference numerical simulation for example, we can identify each grid element as a rectilinear box of fluid.) These parcels are sorted by density, and then distorted (while maintaining a constant volume, and hence not changing the density) to extend over the entire horizontal extent of the flow domain, as shown schematically in the figure. This rearrangement defines the density profile ρ_B, in terms of which the average background potential energy of the system is

$$\mathscr{P}_B = Ri(0)\langle \rho_B(z) z \rangle_z / R. \tag{2.25}$$

$\mathscr{P}_B$ is the minimum possible average potential energy of the entire system, discretized in the particular way defined by the initial choice of parcels. The average available potential energy $\mathscr{P}_A$, which is available to be converted into kinetic energy, is then simply defined as

$$\mathscr{P}_A = \mathscr{P} - \mathscr{P}_B. \tag{2.26}$$

As pointed out by Winters *et al.* (1995), and also implemented by Scinocca (1995), this adiabatic rearrangement is straightforward to implement in a numerical simulation. The fluid is redistributed notionally within the computational domain into the strictly monotonic, stably stratified state with density distribution ρ_B by notionally deforming each of the computational grid boxes into thin sheets of constant-density fluid as shown schematically in figure 3. The average potential energy $\mathscr{P}_B$ of such a configuration may then be computed, and its evolution tracked with time.

We define the average (total) potential energy of the system as

$$\mathscr{P} = Ri(0)\langle \rho z \rangle_{xyz} / R = Ri(0)\langle z \bar{\rho} \rangle_z / R, \tag{2.27}$$

i.e. the evolution of potential energy is entirely determined by the evolution of the vertical profile of mean density. The time evolution of the average total potential

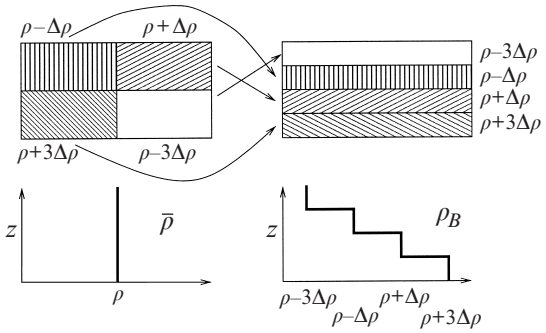

FIGURE 3. Schematic diagram of the adiabatic redistribution of fluid parcels (with densities $\rho \pm 3\Delta\rho$ and $\rho \pm \Delta\rho$) to evaluate the background density distribution ρ_B associated with the average minimal background potential energy $\mathscr{P}_B$ of a flow. Also shown are the vertical distributions of the mean density $\bar{\rho}$ and the background density distribution ρ_B.

energy is governed by the equation

$$\frac{\mathrm{d}}{\mathrm{d}t}\mathscr{P} = \frac{Ri(0)}{R}\langle \rho w \rangle_{xyz} + \hat{\mathscr{D}}_{\mathscr{P}}, \tag{2.28}$$

where $\hat{\mathscr{D}}_{\mathscr{P}}$ is the diffusive irreversible conversion of the fluid's internal energy into potential energy, and is strictly positive, and the hat denotes no normalization by $2\mathscr{K}$. Our domain was sufficiently deep so that to a good approximation $\hat{\mathscr{D}}_{\mathscr{P}}$ was constant, and equal to

$$\hat{\mathscr{D}}_{\mathscr{P}} = Ri(0)/(10RRePr). \tag{2.29}$$

Thus the average potential energy is irreversibly increasing at a constant rate due to diffusion. Within our simulations, this term plays a negligible role in the dynamic evolution of the flow.

On the other hand the buoyancy flux term, $-\hat{\mathscr{H}} = -2\mathscr{K}\mathscr{H}$, where $\mathscr{H}$ is as defined in (2.21) may be positive or negative depending on the particular structure of perturbations, plays a fundamental role in the flow dynamics. The average background potential energy always increases with time, either through mixing or diffusion of the mean fluid density profile, at a rate that is bounded below by $\hat{\mathscr{D}}_{\mathscr{P}}$. Since it is possible by direct calculation to determine continuously the rate at which $\mathscr{P}_B$ is increasing, the evolution equations for the two distinct components of the potential energy density may be written as

$$\frac{\mathrm{d}}{\mathrm{d}t}\mathscr{P}_{\mathscr{A}} = -\hat{\mathscr{H}} - \hat{\mathscr{M}} \equiv \hat{\mathscr{S}}, \tag{2.30}$$

$$\frac{\mathrm{d}}{\mathrm{d}t}\mathscr{P}_{\mathscr{B}} = \hat{\mathscr{M}} + \hat{\mathscr{D}}_{\mathscr{P}}, \tag{2.31}$$

where $\hat{\mathscr{M}}$ is a non-negative quantity which may be identified as the instantaneous mixing rate, and $\hat{\mathscr{S}}$ is (by definition) the instantaneous stirring rate. It is important to appreciate that, in the absence of motion, $\hat{\mathscr{M}} \to 0$, and so 'mixing' as we define it is inherently related to fluid motion.

2.3. *Mixing efficiency*

The instantaneous mixing rate $\hat{\mathscr{M}}$ may be used to define instantaneous and cumulative mixing efficiencies within a shear flow in a manner consistent with definitions used in

experiments (Linden 1979). Conventionally, mixing efficiency is defined as the ratio of the increase in the total potential energy of the system to the work done on the fluid (by the driving mechanism). As mentioned in the introduction, the effective Prandtl number of salt-stratified experiments is appreciably higher than in our numerical calculations, and so the effect of $\mathscr{D}_{\mathscr{P}}$ is appreciably weaker (see (2.29)). As already noted $\mathscr{D}_{\mathscr{P}}$ can be precisely calculated and plays no significant role in the development of mixing within our simulations. Within a salt-stratified fluid, this diffusive term will be even smaller, and diffusive increases in flow potential energy will take place over even longer timescales. Therefore, we choose to remove explicitly contributions due to this term from the numerically calculated average potential energy, thus improving comparison between numerical simulations and experiments.

In experiments, the work done on the fluid is the amount of energy which is pumped into small scales by the breakdown of forced large-scale disturbances, some of which is dissipated, and some of which causes the fluid to mix, and thus increase the potential energy of the system. Clearly, the mixing efficiency must always be less than one, and is typically of the order $0.1 \sim 0.2$. Of great interest is the dependence of the mixing efficiency on the overall stratification of the system (measured by some appropriate Richardson number). Non-monotonicity in this dependence has been observed in many different experiments (Linden 1979; Park *et al.* 1994) in the sense that there is some (non-zero) ambient stratification which maximizes the mixing efficiency. As originally theoretically postulated by Phillips (1972) and Posmentier (1997), and more recently developed by Barenblatt (1993) and Balmforth, Llewellyn Smith & Young (1998), this non-monotonicity is responsible for the evolution of the density field into a layered staircase structure. Through time, the mixing induced by turbulent motions causes the density field to evolve into relatively well-mixed regions separated by appreciably thinner regions of high density gradient. Such density staircases are commonly observed in the oceans, as well as experimentally (Park *et al.* 1994).

To develop an analogous definition of mixing efficiency within an unforced free shear flow, it is sensible to identify the work done on the fluid with the amount of kinetic energy which is irreversibly lost by the fluid. Using (2.30), (2.20) may be rewritten as

$$\sigma(t) = -\mathscr{S} - \mathscr{M} + \mathscr{D}, \tag{2.32}$$

where the mixing rate and stirring rate have been normalized by division by $2\mathscr{K}(t)$. The last two terms describe the rate at which kinetic energy is irreversibly lost from the flow to mixing and to dissipation. Since throughout a simulation each of these terms can be determined at any particular instant, and in general will be functions of time, a natural definition of an instantaneous mixing efficiency $\mathscr{E}_i$ is

$$\mathscr{E}_i \equiv \frac{\mathscr{M}}{\mathscr{M} - \mathscr{D}} < 1. \tag{2.33}$$

It is actually of most interest to understand the cumulative mixing efficiency of a shear flow throughout its evolution, by analogy with experiments. Therefore, we define a cumulative mixing efficiency $\mathscr{E}_c$ as

$$\mathscr{E}_c(t) \equiv \frac{\displaystyle\int_0^t \mathscr{M}(u)\,\mathrm{d}u}{\displaystyle\int_0^t \mathscr{M}(u)\,\mathrm{d}u - \int_0^t \mathscr{D}(u)\,\mathrm{d}u}. \tag{2.34}$$

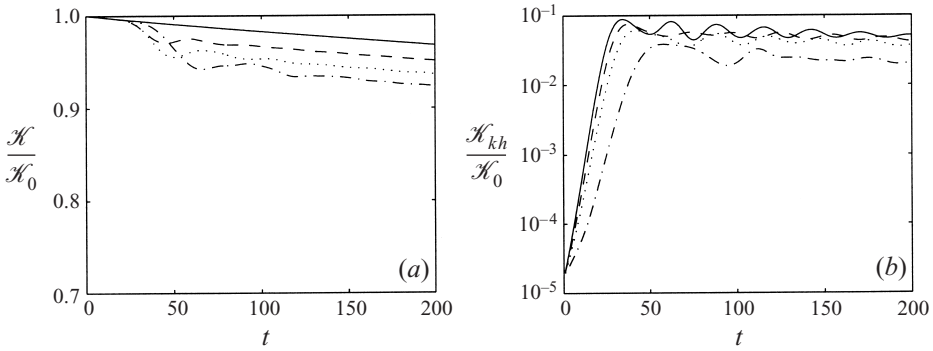

FIGURE 4. Time evolution in an inherently two-dimensional flow of: (*a*) $\mathscr{K}(t)/\mathscr{K}(0)$ (defined by (2.15)); and (*b*) $\mathscr{K}_{kh}(t)/\mathscr{K}(0)$ (defined by (2.15) and (2.18)); for $Ri(0) = 0$ (solid line), $Ri(0) = 0.025$ (dashed line) $Ri(0) = 0.05$ (dotted line) and $Ri(0) = 0.1$ (dot-dashed line).

3. Two-dimensional simulations

We have conducted a sequence of two-dimensional simulations with initial profiles of velocity and density given by (2.1) and (2.2) for comparison with fully three-dimensional simulations. The initial minimum Richardson numbers were set at 0, 0.025, 0.05 and 0.1. We initialized the calculations with a perturbation of the form of the eigenfunction of the most unstable (inviscid) mode of linear theory. Since the behaviour of a two-dimensional KH billow is well understood, the perturbation amplitude was chosen so that, for all calculations $\mathscr{K}_{kh}(0)/\mathscr{K}(0) = 1.9 \times 10^{-5}$, and so the KH billow had a relatively brief linear phase of development. For subsequent comparison with the results of our three-dimensional simulations, we wish to understand the global characteristics of flows restricted to two dimensions (and in particular the mixing efficiency of such flows) so that we can later determine how three-dimensionality crucially modifies flow evolution.

In figure 4(*a*) we plot $\mathscr{K}$ defined by (2.15), normalized with its initial value, against time for each of our simulations. The behaviour of the unstratified simulation (shown with a solid line) is quite straightforward, as $\mathscr{K}$ decreases monotonically due to viscous dissipation. The rate of this decay is quite slow, and clearly does not vary greatly over the time shown (or indeed over significantly longer timescales). Since dissipation is dominated by contributions from small-scales gradients, this implies that there is little small-scale motion within the flow. For the stratified simulations, there is still an underlying trend of decrease in $\mathscr{K}$ due to viscous dissipation, but there is also an oscillation in $\mathscr{K}$ due to the effect of exchanges, both reversible and irreversible, between the kinetic energy and the potential energy of the system.

As the billow rolls up, the buoyancy flux $\mathscr{H}$ is negative, and so the potential energy of the flow increases due to the fluid motion. In figure 5 we plot $\mathscr{P} - \mathscr{D}_{\mathscr{P}}t - \mathscr{P}(0)$ (where t is the time from the start of the simulation and $\mathscr{D}_{\mathscr{P}}$ is as defined in (2.29)) with a solid line, $\mathscr{P}_B - \mathscr{D}_{\mathscr{P}}t - \mathscr{P}_B(0)$ with a dashed line, and $\mathscr{P}_A - \mathscr{P}_A(0)$ with a dotted line. From this figure, it is clear that the initial vortex roll-up is essentially a stirring mechanism, and leads to a significant increase in the average available potential energy $\mathscr{P}_A$. Much of this $\mathscr{P}_A$ is reversibly exchanged back into kinetic energy of the flow, as can be deduced from the fact that the average total potential energy $\mathscr{P}$ subsequently decreases, and the average total kinetic energy $\mathscr{K}$ of the stratified flows actually increases transiently.

This exchange is imperfect, as in a two-dimensional flow at these Reynolds numbers

the dominant mixing process occurs immediately after the roll-up of the primary KH billow (leading to an irreversible increase in $\mathscr{P}_B$) associated with mixing within the statically unstable regions of the flow. There is a significant increase in $\mathscr{P}_A$, which is associated with the re-creation of statically unstable regions within the flow as the KH billow continues to roll up, with the intensity varying with the initial ambient stratification (see figure 5*a*, *c*, *e*). The statically unstable regions at the periphery of the primary billow core can be considered to have a finite lifetime, which is of the order of 10–20 non-dimensional time units. Since (as can be seen in figure 1*b*) the statically unstable regions are of the same order as the initial density layer half-depth (and hence, from (2.1) and (2.2) of the same order as the initial shear layer half-depth d) the non-dimensional timescale for diffusion to strongly affect these statically unstable regions is of the order of $RePr = 750$, appreciably longer than their numerically observed lifetime. Therefore, the available potential energy $\mathscr{P}_A$ derives motions appreciably more rapidly than diffusion can affect the flow, and so we feel confident that density diffusion does not play a significant dynamical role in the development of motions within these regions.

Physically, the development of the KH instability leads to a significant broadening in the depth of the shear layer, indicative of an overall redistribution of the average total kinetic energy from the mean flow into the perturbation. The process of roll-up of the KH billow also strongly modifies the density distribution. A layer of intermediate density is formed by the irreversible mixing induced by the creation of statically unstable regions during the roll-up of the primary KH billow. This intermediate layer is separated by relatively thin regions of high density gradient from the fluid above and below the mixing layer.

In figure 4(*b*), we plot the time evolution of the two-dimensional perturbation kinetic energy $\mathscr{K}_{kh}$, normalized by the initial value of the average total kinetic energy, i.e. $\mathscr{K}(0)$. In each case the perturbations undergo essentially exponential growth initially, with the growth rate and peak amplitude decreasing with stratification as is expected. Subsequently, the amplitude of the primary billow oscillates and the billow nutates slightly, with $\mathscr{K}_{kh}$ being maximum when the billow is closest to circular. This oscillation is due to a reversible exchange of kinetic energy between the mean field and the perturbation.

In attempting to consider quantitatively the issue of mixing efficiency, it is important to remember that these two-dimensional flows never become turbulent in any real sense, and hence the dissipation rate of the total kinetic energy $\mathscr{D}$ is always quite small. Therefore, from our definition (2.34) of the cumulative mixing efficiency $\mathscr{E}_c$, we expect $\mathscr{E}_c \sim 1$ for these two-dimensional flows. This is indeed the case, as shown in figure 5(*b*, *d*, *f*). Two points should be noted. First, the most significant mixing events (and thus peaks in $\mathscr{E}_i$, also plotted in the figures) occur after the KH billow saturates. These events correspond to the mixing associated with the statically unstable regions induced within the billow itself, and take significant periods of time to complete. After these mixing events are completed, the mixing efficiency falls until statically unstable regions once again develop within the primary billow core, as the billow continues to rotate. New statically unstable regions then in turn lead to mixing events, and thus another peak in $\mathscr{E}_i$. Secondly, we find that $\mathscr{E}_c$ is a monotonically increasing function of $Ri(0)$ for the three flows which we have considered, although the qualitative structure of the time variation of $\mathscr{E}_c$ varies little with $Ri(0)$. This is not entirely surprising, as the flows are never turbulent, and the dissipation rate is not a strong function of $Ri(0)$, whereas the mixing rate $\mathscr{M}$ increases strongly with stratification. The dominant mechanism for mixing is associated with the roll-up of the billow itself.

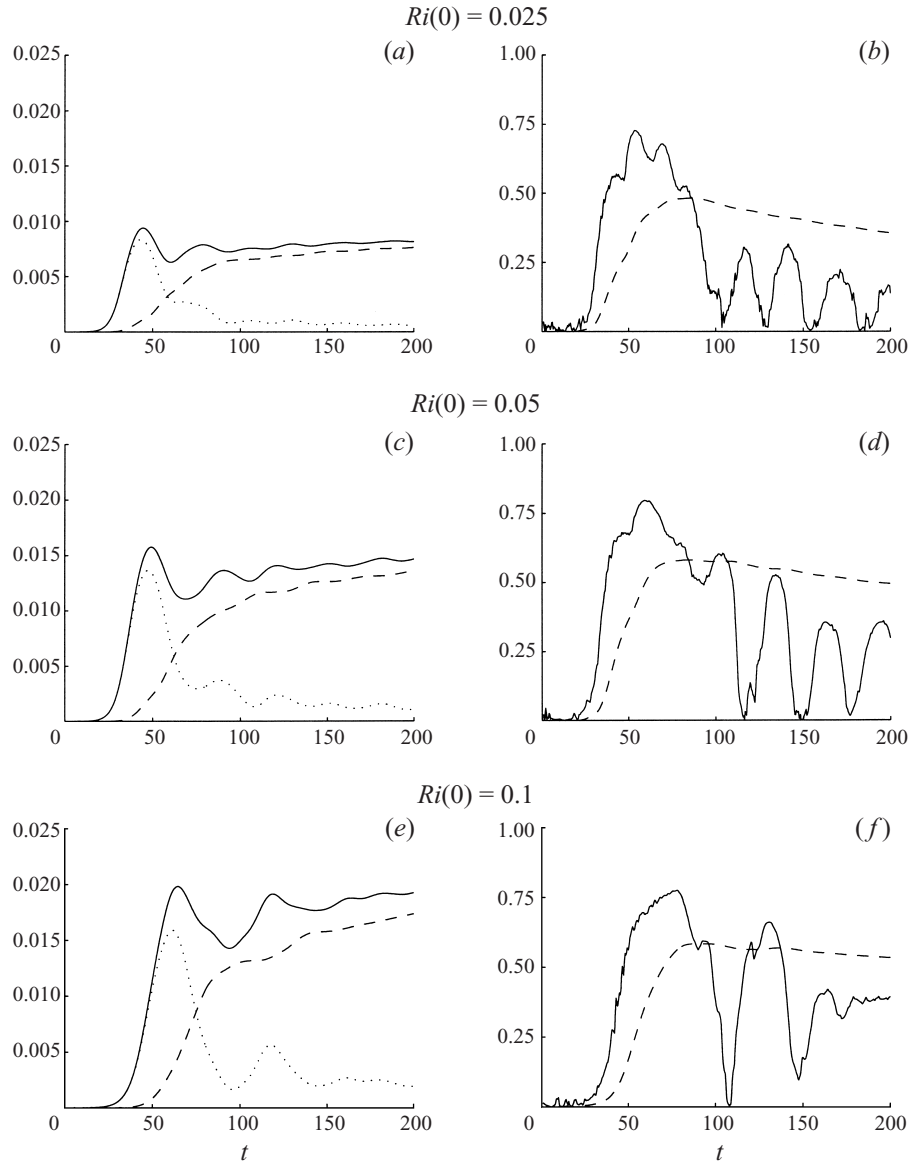

FIGURE 5. Time variation of $\mathscr{P}(t)-\mathscr{D}_{\mathscr{P}}t-\mathscr{P}(0)$ (defined by (2.27) and (2.29)) (solid line), $\mathscr{P}_A(t)-\mathscr{P}_A(0)$ (defined by (2.26)) (dotted) and $\mathscr{P}_B(t)-\mathscr{D}_{\mathscr{P}}t-\mathscr{P}_B(0)$ (defined by (2.25)) (dashed) for inherently two-dimensional simulations with (*a*) $Ri(0) = 0.025$; (*c*) 0.05; (*e*) 0.1, compared with the time variation of $\mathscr{E}_i$ (defined by (2.33)) (solid line) and $\mathscr{E}_c$ (defined by (2.34)) (dashed) for inherently two-dimensional simulations with (*b*) $Ri(0) = 0.025$; (*d*) 0.05; (*f*) 0.1.

From these calculations, it would appear that a natural instant of time at which to consider the structure of the flow is the time at which $\mathscr{K}_{kh}$ is a maximum. We shall refer to this time as $t_{2d\,\max}$. In figure 6 we plot the distribution of the spanwise vorticity for each of the different simulations at the relevant time $t_{2d\,\max}$. For each of the stratified simulations we shade the statically unstable regions of the flow which have developed due to the roll-up of the primary KH billow. When $Ri(0) = 0$, the structure of the flow is relatively simple, with the vorticity in the flow now concentrated in an elliptical

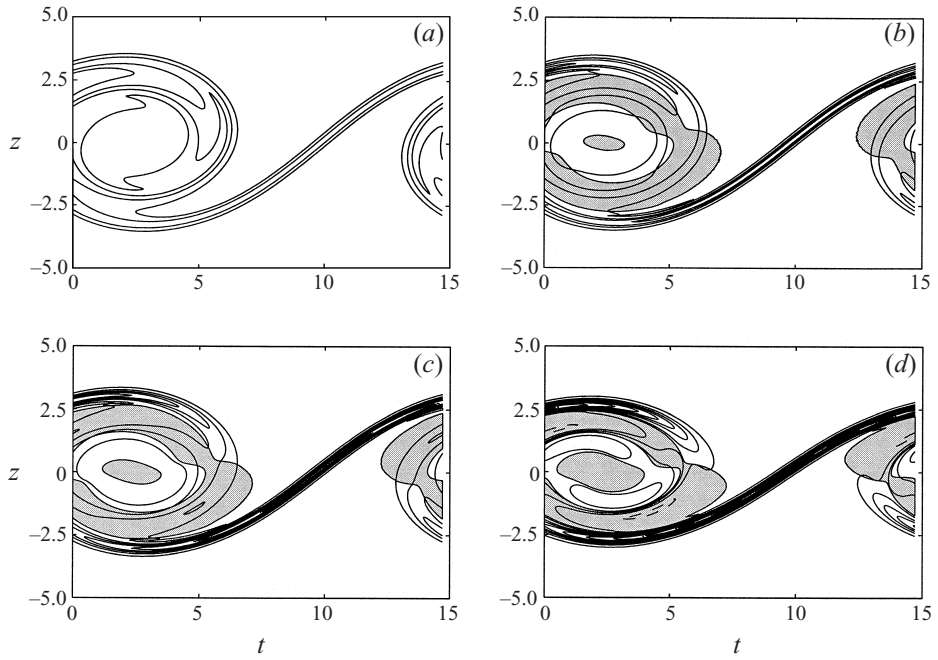

FIGURE 6. Contours of spanwise vorticity at time $t_{2d\,\max}$ for inherently two-dimensional simulations with (*a*) $Ri(0) = 0$, $t_{2d\,\max} = 34.0$; (*b*) 0.025, $t_{2d\,\max} = 38.2$; (*c*) 0.05, $t_{2d\,\max} = 42.0$; (*d*) 0.1, $t_{2d\,\max} = 57.6$. Statically unstable regions of the flow are shaded.

region, which nevertheless extends over a greater width than the original shear layer. This spreading of the vorticity can be thought of as leading to a thickening of the mixing layer region. Momentum has been redistributed through a greater depth of the flow than in the initial (laminar) flow, but the flow remains highly ordered.

With $Ri(0) \neq 0$ however, the evolution of the spanwise vorticity field is markedly different, as there are now potential sources and sinks of spanwise vorticity, due to baroclinic torques which in the Boussinesq approximation are driven by streamwise gradients in the density field (see Staquet 1995 for a detailed discussion). On a large scale, also note that the vertical extent of the vortical region (the KH billow) is somewhat reduced by the influence of the vertical density stratification. From the shading in figure 6(*b–d*), the periphery of the primary billow core is the dominant site of static instability. (See KP85 and KP91 for a fuller discussion, where these regions are referred to as super adiabatic regions or SARS.) These convectively unstable regions are deepest at the upstream edge of the upper periphery of the primary KH billow, and at the downstream edge of the lower periphery of the primary KH billow.

4. Secondary stability analysis

We conducted a secondary stability analysis of the non-parallel flows shown in figure 6 using the methodology described in KP85 and KP91. Fundamentally, we make four assumptions, which reduce the stability analysis to an eigenvalue problem. First, we assume that it is possible initially to decompose the total flow into a quasi-steady, two-dimensional part (figure 6), and a small-amplitude three-dimensional part. Secondly, we assume that both the background flow and the three-dimensional perturbation may be considered periodic in the streamwise direction, with some characteristic length

scale L_y, chosen to be the wavelength of the most unstable mode of linear theory. Thirdly, we assume that the three-dimensional disturbances have significant amplitude over a finite vertical extent, and so on the basis of Floquet theory, (see, for example, Bender & Orszag 1978) the spanwise part of the three-dimensional perturbations may be separated from the streamwise-vertical two-dimensional part. Our final assumption, which requires detailed knowledge of the evolution of the (inherently) unsteady two-dimensional background flow, is to suppose that the two-dimensional background flow is steady. We can then assert that the temporal and spatial parts of $\boldsymbol{u}_{3d}$ and ρ_{3d} are separable, and so finally, we may write the three-dimensional perturbation as

$$\boldsymbol{u}_{3d}(x, y, z, t) = \boldsymbol{u}^{\dagger}_{3d}(y, z) \exp\left[\mathrm{i}\gamma x + nt\right], \tag{4.1}$$

$$\rho_{3d}(x, y, z, t) = \rho^{\dagger}_{3d}(y, z) \exp\left[i\gamma x + nt\right]. \tag{4.2}$$

where

$$n \equiv n_r + \mathrm{i}n_i. \tag{4.3}$$

In all cases studied, we found that the growth rate for any given group of modes (in a harmonic sequence) was largest when $n_i = 0$, which is the case on which we focus here.

The validity of the last separability assumption (which allows us to turn the initial value problem into an appreciably simpler eigenvalue problem) requires the growth rate n_r of the three-dimensional perturbation to be appreciably larger than the rate at which the background flow evolves, as discussed in detail in Smyth & Peltier (1994), and more fully in Potylitsin & Peltier (1998). In the particular case under consideration, the Reynolds number of the flow is sufficiently large so that the variation of the two-dimensional flow is dominated by the variation in the two-dimensional perturbation associated with the KH billow. As can be seen from the evolution of $\mathscr{K}_{kh}$ in figure 4*b*, after the primary KH billow has saturated, the normalized growth rate σ_{kh} of the KH billow, defined as

$$\sigma_{kh} = \frac{1}{2\mathscr{K}_{kh}} \frac{\mathrm{d}}{\mathrm{d}t} \mathscr{K}_{kh}, \tag{4.4}$$

is bounded above by 0.02 for all times after the maximum amplitude of the perturbation has been attained for all of our simulations. To ensure that the separability assumption is justified, we must then disregard any predicted three-dimensional instabilities unless the growth rates associated with them are such that

$$n_r \gg |\sigma_{kh}|. \tag{4.5}$$

The perturbation defined in (4.1) and (4.2) can then be approximated using an appropriately truncated Galerkin representation (see KP85), and then, upon linearization of the governing equations about the two-dimensional background flow, the stability problem reduces to a matrix eigenvalue problem which may be solved using conventional techniques. The method not only yields values for the spanwise wavenumber γ and growth rate n_r, but also the spatial distribution of the perturbation, $\boldsymbol{u}^{\dagger}_{3d}(y, z)$ and $\rho^{\dagger}_{3d}(y, z)$ and hence the average three-dimensional perturbation kinetic energy density $\mathscr{K}_{3d}$, defined in (2.19).

In general, $\mathscr{K}_{3d}$ associated with any particular mode may be considered to be the average of a two-dimensional quantity $K_{3d}(y, z)$, defined by

$$\mathscr{K}_{3d} = \tfrac{1}{2}\langle(|u^{\dagger}_{3d}|^2 + |v^{\dagger}_{3d}|^2 + |w^{\dagger}_{3d}|^2)\rangle_{yz}, \tag{4.6}$$

$$\equiv \langle K_{3d}(y, z)\rangle_{yz}. \tag{4.7}$$

$Ri(0)$	γ	n_r	$\mathscr{S}\mathscr{H}\mathscr{B}_{3d}$	$\mathscr{S}\mathscr{H}\mathscr{K}\mathscr{H}_{3d}$	$\mathscr{S}\mathscr{H}_{3d}$	$\mathscr{H}_{3d}$	$\mathscr{S}\mathscr{T}_{3d}$	$\mathscr{D}_{3d}$
0.000	0.9	0.0849	0.1051	−0.0159	0.0892	0	0.0006	−0.0049
0.000	2.5	0.1471	0.1241	0.0174	0.1415	0	0.0192	−0.0136
0.025	2.8	0.1299	0.1068	−0.0040	0.1028	0.0256	0.0187	−0.0172
0.050	3.3	0.1796	0.1149	−0.0239	0.0910	0.0911	0.0191	−0.0216
0.100	4.6	0.2565	0.0780	−0.0021	0.0759	0.1738	0.0473	−0.0405

TABLE 1. Properties of the most unstable three-dimensional modes at varying $Ri(0)$.

By investigating the spatial structure of K_{3d}, we are able to identify the dominant sites of three-dimensionalization predicted by the stability analysis. Furthermore, as discussed in KP91, since we know the three-dimensional perturbation fields, we are able to evaluate the terms on the right-hand side of (2.23) associated with a particular three-dimensional perturbation. Such terms also allow us to perform a useful independent check on the accuracy of our calculations, i.e. to check that $n_r = \sigma_{3d}$, and so

$$n_r = \mathscr{S}\mathscr{H}\mathscr{B}_{3d} + \mathscr{S}\mathscr{H}\mathscr{K}\mathscr{H}_{3d} + \mathscr{S}\mathscr{T}_{3d} + \mathscr{H}_{3d} + \mathscr{D}_{3d} \tag{4.8}$$

is satisfied, where each of the terms is determined, analogously to $\mathscr{K}_{3d}$ in (4.6), directly from the three-dimensional perturbation given in (4.1) and (4.2). For all the results presented in this paper, (4.8) is satisfied to better than 1%.

For each flow, we found a weak dependence of n_r on γ, provided γ is sufficiently large. The wavenumber γ at which maximal growth is predicted to occur does increase with increasing stratification however, varying from $\gamma = 2.5$ for the unstratified flow to $\gamma = 4.6$ for the flow with $Ri(0) = 0.1$, as presented in table 1. The values of the various terms on the right-hand side of (4.8) are also shown, where $\mathscr{S}\mathscr{H}_{3d} = \mathscr{S}\mathscr{H}\mathscr{B}_{3d} + \mathscr{S}\mathscr{H}\mathscr{K}\mathscr{H}_{3d}$ is the total shearing contribution to growth. The wavenumbers which are predicted imply that the characteristic spanwise scale of secondary instability should be significantly less than the streamwise wavelength of the characteristic KH billow.

For the stratified flows, the wavelength of the most unstable mode is of the same order as the depth of the convectively unstable region around the periphery of the primary KH billow core. Klaassen & Peltier (1985*b*) found that the primary effect of variations in the characteristics of secondary instabilities with the fluid's Prandtl number could be traced to variations in the depth of these convective regions. Within their calculations, the variations in the depths of these convective regions could be attributed to the varying lengths of time that primary KH billows took to saturate. This is reasonable, since the stability analysis assumes that the flows (shown in figure 6) remain frozen in time. Provided the development of the primary KH instability is sufficiently rapid so that the effects of diffusion of the density field are small (which it is for sufficiently high Re and sufficiently low $Ri(0)$, the characteristic scale of the convectively unstable regions will be of the same order as the initial characteristic depth of density variation, which scales with the shear layer depth (see (2.1) and (2.2), remembering that $R = 1.1$ in our simulations).

In general, there is a slight change in the form of the growth rate curve around $\gamma = 0.9$, with a lesser growth rate than at the higher wavenumbers. Furthermore, the maximal growth rate of the secondary instability appears to be a strong function of $Ri(0)$, with the initially surprising result that increasing the background stable stratification actually increases the growth rate of the secondary instability.

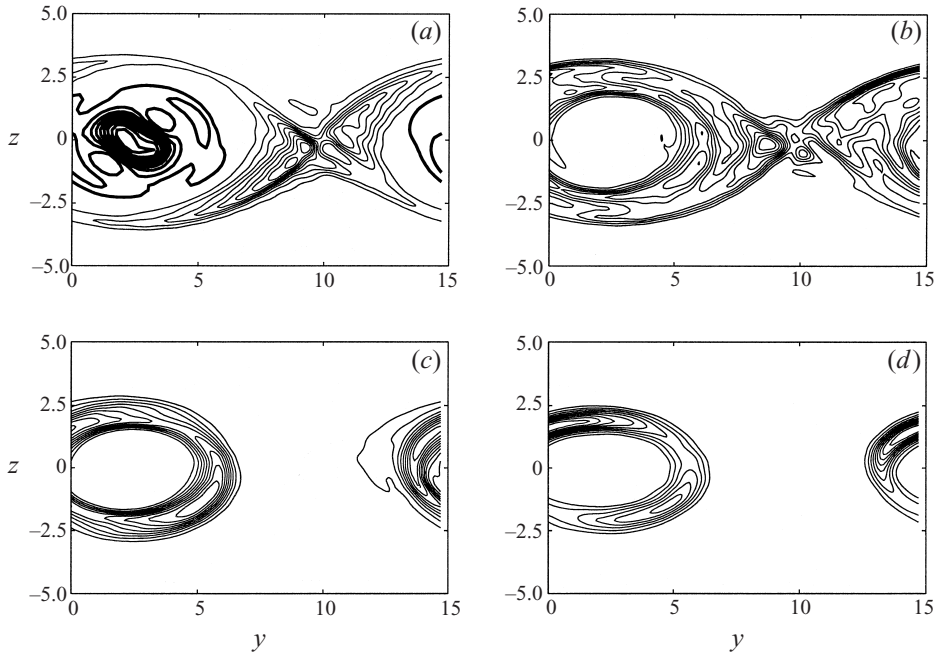

FIGURE 7. Contours of K_{3d} (as defined in (4.7)) for the most unstable mode in flows with (*a*) $Ri(0) = 0$ (thin solid lines show the most unstable (hyperbolic) mode with $\gamma = 2.5$, thick solid lines show the most unstable elliptical mode with $\gamma = 0.9$); (*b*) $Ri(0) = 0.025$; (*c*) 0.05; (*d*) 0.1.

4.1. *Unstratified secondary instability structures*

In figure 7(*a*), we plot (with thin solid lines) contours throughout the computational domain of K_{3d} defined by (4.7) for the most unstable eigenmode of the unstratified simulation with $Ri(0) = 0$. As has been noted previously by KP91 the most important detail to note is that the energy associated with this mode is predominantly located in the braid region in the case of the unstratified flow. There is some amplitude of perturbation around the periphery of the KH billow, but there is essentially none in the billow core. This braid-centred instability, which was identified by KP91, dominates the high-wavenumber part ($\gamma > 1$) of the three-dimensional instability spectrum for unstratified flows, and appears to be fundamentally unrelated to the elliptical mode of instability for flows with sufficiently high Reynolds numbers. Because the streamlines of the flow induced by the primary KH billow are locally hyperbolic in the vicinity of the braids, we will henceforth refer to the basic mode as constituting a hyperbolic instability.

This technique also predicts the development of instabilities which have similar structure to the elliptical instability of Pierrehumbert & Widnall (1982) but only at lower growth rate, with the maximal growth rate occurring for modes of this structure having spanwise wavenumber $\gamma = 0.9$, as listed in table 1. In figure 7(*a*), we also plot K_{3d} for this mode with thick solid lines, which has growth rate less than 60% of the most unstable braid-centred mode with wavenumber $\gamma = 2.5$. Clearly, the two modes are localized in distinct parts of the flow. Based upon our analyses of the flow associated with the maximum-amplitude unstratified KH billow with $Re = 750$, the band of spanwise wavenumbers susceptible to this elliptical instability is relatively narrow. The most unstable mode has a wavenumber that is appreciably smaller than

the most unstable braid-centred or hyperbolic instability. This result is consistent with the results of Smyth & Peltier (1994), developing KP91.

The dominant physical source for the growth of perturbation kinetic energy for both the braid-centred mode and the core-centred mode is identified by considering the relative magnitudes of the various terms in table 1. By far the dominant source of energy is the background shear (consistently with the observations of KP91) and the flow directly associated with the two-dimensional KH billow, though essential to the growth of the perturbation, fulfils a role which is appropriately described as 'catalytic'. Physically, both instabilities are translative in nature, since the core-centred perturbation corresponds to a spanwise periodic raising and lowering of the primary billow core, while the distinct, significantly more unstable hyperbolic instability corresponds to a spanwise periodic raising and lowering of the braid region normal to its angle of orientation.

Although the predictions of this theory are only valid during the linear phase of (secondary) flow development, the predicted hyperbolic instability structures which develop within the braid are of a form that is conducive to further growth in amplitude as their development becomes nonlinear. These structures (i.e. streamwise vortex tubes which develop in the braid region and are aligned with the streamwise principal direction of strain) are naturally coherent in a way such that $v_{3d}w_{3d} < 0$, and thus can continue to extract energy efficiently from the background shear flow as the amplitude of the perturbation increases. The development of the hyperbolic instability does, of itself, fully explain the appearance of the observed streamwise tubes at finite amplitude (see Potylitsin & Peltier 1998 for an explicit demonstration of this fact based solely upon the non-separable linear stability analysis). The behaviour of the flow is dependent on the local characteristics in the vicinity of the braid, with no external forcing (or supply of vorticity) from neighbouring billows being required, since streamwise vorticity is in the nature of the perturbation structure itself, and can be further supplied by tilting of the spanwise vorticity of the braid.

4.2. *Stratified secondary instability structures*

In figure 7(*b–d*), we plot contours throughout the computational domain of K_{3d} defined by (4.7) for the most unstable eigenmode for each of our stratified flow calculations. As $Ri(0)$ increases, there is a clear transition to a fundamentally different structure from the braid-centred mode which we predict to dominate the development in an unstratified flow. For the simulations with $Ri(0) = 0.05$ and $Ri(0) = 0.1$, the structure of K_{3d} is very similar, with dominant contributions to the perturbation kinetic energy of the mode from two regions. One is below and slightly towards the leading edge of the primary billow and the other is above and slightly towards the trailing edge. These results are consistent with the lower resolution calculations of KP85 and KP91. Importantly, these regions of strong perturbation kinetic energy appear to lie within the statically unstable regions induced by billow roll-up as shown in figure 6. For these two higher values of $Ri(0)$, there is negligible contribution to the kinetic energy of this mode in the braid region. However, for $Ri(0) = 0.025$, there appears to be a hybrid instability, combining both the braid-centred structure of the instability in the unstratified case with significant contributions from the statically unstable regions on the periphery of the primary billow core. The quantitative integrated data for the various contributions to growth is also presented in table 1.

The net effect of all these contributions is a non-monotonic dependence of the predicted growth rate of the most unstable three-dimensional perturbation with Richardson number (principally due to the increased influence of the buoyancy

flux term $\mathscr{H}_{3d}$). As $Ri(0)$ increases, the wavenumber of the most unstable mode increases. As this implies a transition of the characteristic motion to smaller scales, the dissipation $\mathscr{D}_{3d}$ also increases with $Ri(0)$. The total absolute effect of the shearing contributions decreases with increasing $Ri(0)$. In all cases the shearing contribution associated with the extraction of energy from the mean background field is much larger than the shearing contribution that extracts energy from the two-dimensional flow associated with the KH billow, i.e. $\mathscr{S}\mathscr{H}\mathscr{B}_{3d} \gg |\mathscr{S}\mathscr{H}\mathscr{K}\mathscr{H}_{3d}|$. Also, as $Ri(0)$ increases, the effective contribution of the buoyancy flux term $\mathscr{H}_{3d}$ increases. Perhaps somewhat more surprising is the fact that the straining contribution $\mathscr{S}\mathscr{T}_{3d}$ is substantially larger at high $Ri(0)$. This is due to the increased anisotropy in the velocity field, with $|w^{\dagger}_{3d}| > |v^{\dagger}_{3d}|$.

This anisotropy occurs because the presence of statically unstable layers induces very large values of perturbation vertical velocity in the statically unstable regions, particularly for the more strongly stratified simulations (with $Ri(0) = 0.05$ and 0.1). These vertical velocities are predicted to be appreciably larger in amplitude than in the unstratified flow. Essentially, the perturbation is organized so as to extract efficiently some of the available potential energy $\mathscr{P}_A$ which, on the basis of our two-dimensional calculations, is stored in the statically unstable regions of the density distribution, and to convert it into perturbation kinetic energy.

To do this implies significant vertical velocity within the statically unstable regions, associated physically with convective overturning. This localization of significant vertical velocity in these statically unstable regions then affects all the other mechanisms for energy growth of the perturbation, even after the available potential energy which was stored in the statically unstable density distribution has been converted into perturbation kinetic energy, and through irreversible mixing processes, into background potential energy $\mathscr{P}_B$. Furthermore, since we have assumed explicitly (see (4.1)) that the perturbation is periodic in the spanwise direction, this significant vertical velocity of the perturbation is also varying periodically in the spanwise direction. Therefore, the perturbation which is predicted to be most unstable in a stratified flow induces significant streamwise vorticity in the regions around the periphery of the primary billow core.

The effect of the development of these large-amplitude vertical velocity perturbations is naturally most marked on the buoyancy flux contribution $\mathscr{H}_{3d}$. As the stratification increases, both $\rho^{\dagger}_{3d}$ and $w^{\dagger}_{3d}$ increase in amplitude. The natural motion of the system is to transform the available potential energy stored in the statically unstable regions into kinetic energy of the perturbation, which requires that the buoyancy flux is positive in the statically unstable regions, with largest amplitude where $\rho^{\dagger *}_{3d}$ and $w^{\dagger}_{3d}$ are best (negatively) correlated. This occurs towards the leading edge of the lower statically unstable region, and towards the trailing edge of the upper statically unstable region. This combination of perturbation density and perturbation velocity implies the occurrence of a fully three-dimensional convective overturning in this region, with spanwise wavenumber γ, further evidence for the onset of streamwise vortices in these regions.

The selection of the regions towards the leading edge beneath the billow core, and towards the trailing edge above the billow core is due to two related factors. First, these localities are regions of relatively high velocities, as it is in these regions of the flow that the rolling-up of the primary billow core is causing entrainment of surrounding fluid into the primary billow, and so horizontal velocity perturbations in particular are encouraged in these regions. Also, in these regions the statically unstable layer is at its deepest, and so (as discussed in KP85) the local Rayleigh

number is largest, and therefore the flow is most prone to convective motions, with attendant vertical velocity perturbation. On the other hand, for the more strongly stratified flows, there is a relatively strong stratification in the braid region of the flow, and hence vertical and (to a lesser extent) horizontal velocity perturbations are suppressed. For the more weakly stratified simulation (i.e. $Ri(0) = 0.025$) this effect is not pronounced, and so there is still significant velocity perturbation in the braid region, and the growing perturbation has many of the characteristics of the unstratified hyperbolic instability.

5. Three-dimensional simulations

We conducted four fully three-dimensional nonlinear direct numerical simulations of shear layer evolution, with $Ri(0) = 0$, 0.025, 0.05 and 0.1. In each case, the calculations were initialized by superimposing on the background flow a small-amplitude perturbation with structure determined by the most unstable mode of linear theory, exactly as in the two-dimensional calculations discussed in § 3, i.e. $\mathscr{K}_{kh}(0)/\mathscr{K}(0) = 1.9 \times 10^{-5}$. We also applied a small-amplitude isotropic noise field to the spanwise velocity scaled so that $\mathscr{K}_{3d}(0)/\mathscr{K}(0) = 1 \times 10^{-5}$. It is important to appreciate that the three-dimensional perturbations are not tuned in any way to the theoretical predictions of the previous section.

In figure 8 we plot, for each of the simulations, the average total kinetic energy $\mathscr{K}$ (defined in (2.15)), the average kinetic energy associated with the spanwise-averaged perturbation $\mathscr{K}_{kh}$ (defined in (2.18)), and the average kinetic energy associated with the three-dimensional perturbation away from this spanwise-average $\mathscr{K}_{3d}$ (defined in (2.19)). In each case the average energies are normalized by the initial value of $\mathscr{K}(0)$.

By direct comparison with the diagrams shown in figure 4, it is apparent that the evolution of the three-dimensional flows can be considered as passing through four distinct phases. First, there is a period of growth of the two-dimensional perturbations, at the expense of the (appreciably) weaker three-dimensional perturbations. During this period, in each case, the evolution of the fully three-dimensional simulation was virtually indistinguishable from the evolution of the equivalent two-dimensional simulation, and the three-dimensional motions actually decayed in intensity. Therefore, this first phase should be thought of as one of inherently two-dimensional development.

The second stage of the flow evolution starts exactly when the primary KH billow has saturated, i.e. the moment at which the spanwise-averaged kinetic energy $\mathscr{K}_{kh}$ is a maximum (the time $t_{2d\max}$ as marked on figure 8 with an appropriate symbol). In each of the four cases which we studied, the three-dimensional perturbations immediately started to amplify upon saturation of the primary KH billow. (cf. Metcalfe *et al.* 1987 for an unstratified flow). This justifies our choice in § 4 of the time $t_{2d\max}$ as an appropriate time for analysis of the stability of the two-dimensional flow. Because of the small initial amplitude of the three-dimensional perturbations, the evolution of the total kinetic energy $\mathscr{K}$ and the spanwise-averaged perturbation kinetic energy $\mathscr{K}_{kh}$ was very similar to the evolution in the equivalent two-dimensional flow. Although three-dimensional motions do exist, they are parasitic on the background flow, and do not cause the bulk characteristics of the total flow to deviate significantly from the equivalent two-dimensional flow. In particular, $\mathscr{K}_{kh}$ oscillates, indicating oscillation and nutation of the primary billow core.

Eventually, in all four flows, the evolution of the average total kinetic energy $\mathscr{K}$ in the three-dimensional flow starts to deviate significantly from the evolution of $\mathscr{K}$ in

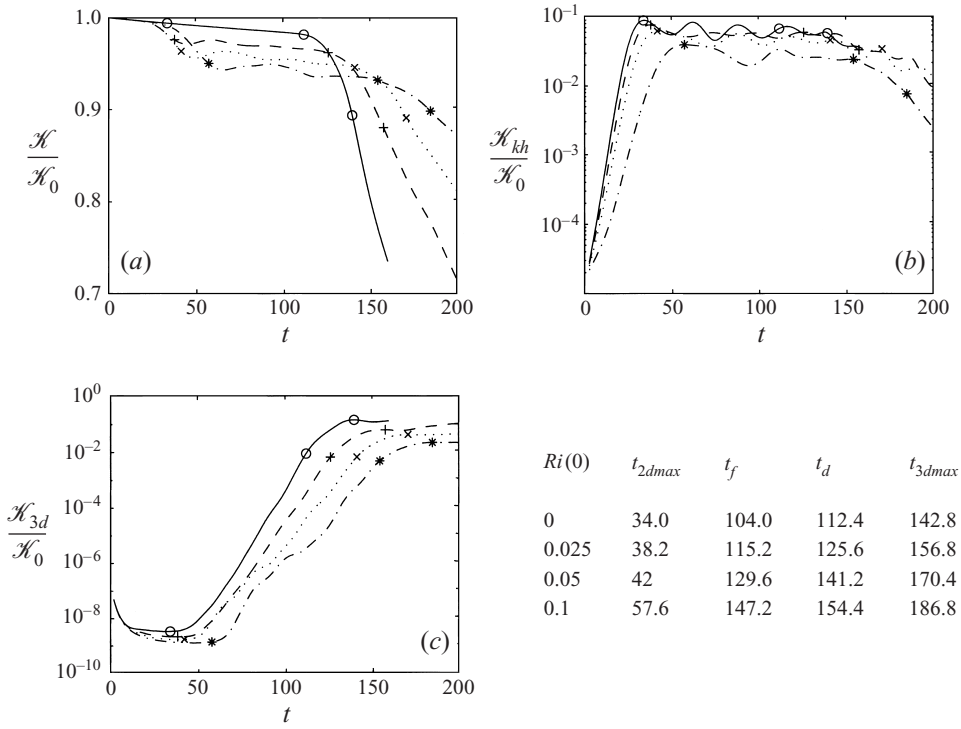

$Ri(0)$	t_{2dmax}	t_f	t_d	t_{3dmax}
0	34.0	104.0	112.4	142.8
0.025	38.2	115.2	125.6	156.8
0.05	42	129.6	141.2	170.4
0.1	57.6	147.2	154.4	186.8

FIGURE 8. Time evolution in an inherently three-dimensional flow of: (*a*) $\mathscr{K}(t)/\mathscr{K}(0)$ (defined by (2.15)); (*b*) $\mathscr{K}_{kh}(t)/\mathscr{K}(0)$ (defined by (2.15) and (2.18)); and (*c*) $\mathscr{K}_{3d}(t)/\mathscr{K}(0)$ (defined by (2.15) and (2.19)) for $Ri(0) = 0$ (solid line), $Ri(0) = 0.025$ (dashed line), $Ri(0) = 0.05$ (dotted line) and $Ri(0) = 0.1$ (dot-dashed line). The characteristic times given in the table are marked with a circle ($Ri(0) = 0$), a plus ($Ri(0) = 0.025$), a cross ($Ri(0) = 0.05$) or an asterisk ($Ri(0) = 0.1$).

the equivalent two-dimensional flow. This change in behaviour during this third stage of the flow evolution is associated with the three-dimensional motions achieving an amplitude which is sufficiently large to have a non-trivial effect on the global flow, and may be thought of as presaging the transition of the flow to turbulent motion, a transition which is inherently three-dimensional. The total viscous dissipation increases markedly, thus leading to an appreciably more rapid decrease in the average total kinetic energy $\mathscr{K}$. On the figures for the various energies we have marked the time t_d at which the normalized dissipation rate of the total kinetic energy $\mathscr{D}$ defined in (2.21) is double its initial value. Though a largely arbitrary subdivision, after this time the flow is inherently three-dimensional, the viscous dissipation continues to increase, and small scales spread throughout the flow. Therefore, we use this time t_d as an indicator of the transition to turbulence within the flow.

This transition takes a finite time, which is only a weak function of $Ri(0)$. Ultimately, at a time $t_{3d\,\max}$ (also marked on figure 8) the three-dimensional motions saturate. This time delimits the start of the fourth stage of the flow development, namely a period of intense three-dimensional motions. After this time, the flow is highly disordered, with the (extremely energetic) three-dimensional motions undergoing a slow decay. At time $t_{3d\,\max}$, $\mathscr{K}_{3d}$ is between 2% (for $Ri(0) = 0.1$) and 12% (for $Ri(0) = 0$) of the initial average total kinetic energy $\mathscr{K}(0)$. Importantly, as $Ri(0)$ increases, the amount of dissipation of the average total kinetic energy $\mathscr{K}$ decreases.

There is also a clear progression in the evolution of the potential energy of the

three stratified flows which we have modelled during these four different stages of flow evolution. In figure 9, we plot the increase in the average total potential energy $\mathscr{P}$, the increase in the average available potential energy $\mathscr{P}_A$ and the increase in the average background potential energy $\mathscr{P}_B$ (as defined in § 2) against time for the three stratified flows. The significant times $t_{2d\max}$, t_d and $t_{3d\max}$ are marked on figure 9 by vertical thick dotted lines. As before (cf. figure 5) for clarity, we subtract the underlying increase in average potential energy due to purely diffusive effects from $\mathscr{P}$ and $\mathscr{P}_B$, and also the initial values of the various potential energies.

As with the evolution of the kinetic energy of the flow, the evolution of the average potential energy of each of the stratified flows during the development of the primary KH billow is essentially indistinguishable in two and three dimensions (cf. figure 5). Also, during the second stage of initial amplification of the three-dimensional perturbations (i.e. when $t_{2d\max} < t < t_d$) there is little difference between the evolution of the potential energy in a three-dimensional flow and in a two-dimensional flow. The period of significant three-dimensional perturbation growth in our two more strongly stratified calculations starts during a stage of irreversible mixing (and thus increase in the background potential energy $\mathscr{P}_B$) but then continues during a period of relatively small change in the background potential energy $\mathscr{P}_B$. This observation suggests that the initial growth mechanism which triggers the onset of three-dimensional motions in a stratified flow is intimately related to perturbations in the density field. However, the subsequent amplification of the three-dimensional structures to finite amplitude is largely dependent on processes which do not involve density effects.

By comparing figures 8 and 9, we see that the total potential energy of the system starts to increase significantly at essentially the same time as the total kinetic energy starts to decrease significantly. Importantly, the increase in potential energy is not principally due to a reversible exchange between the kinetic energy and (available) potential energy reservoirs, but is associated with significant increases in the background potential energy $\mathscr{P}_B$ of the flow, further indication of significant mixing occurring within the fluid. The proportional amount by which $\mathscr{P}_B$ increases decreases as $Ri(0)$ increases. Enhanced irreversible mixing continues during the post-transition fourth stage of flow development, after the three-dimensional perturbations have attained their maximum amplitude.

To illustrate this, in figure 9, we also plot the cumulative and instantaneous mixing efficiencies (i.e. $\mathscr{E}_c$ and $\mathscr{E}_i$ respectively, defined by (2.34) and (2.33)) for each of the three stratified flows in our three-dimensional simulations. During transition both mixing efficiencies undergo significant reductions, differing qualitatively from the two-dimensional results presented in § 3 (cf. figure 5), as the effect of enhanced dissipation greatly outweighs the effect of enhanced mixing. Ultimately, the mixing efficiency tends towards a new, significantly reduced value.

The first two stages of initial primary billow development and three-dimensional perturbation growth have mixing characteristics virtually identical to those of the equivalent two-dimensional flow. Significant irreversible mixing occurs during, and particularly immediately after, the roll-up of the primary billow core, with relatively small amounts of associated dissipation. Thus this mixing is quite an efficient process, with $\mathscr{E}_c \sim 0.5$. However, when the flow evolution of our three-dimensional simulations deviates substantially from the two-dimensional flow evolution, the mixing efficiency is significantly reduced.

When the flow is undergoing transition (i.e. $t_d < t < t_{3d\max}$) in each case the cumulative mixing efficiency decreases markedly. Subsequently to the three-dimensional perturbations reaching maximum amplitude, when the flow is undergoing turbulent

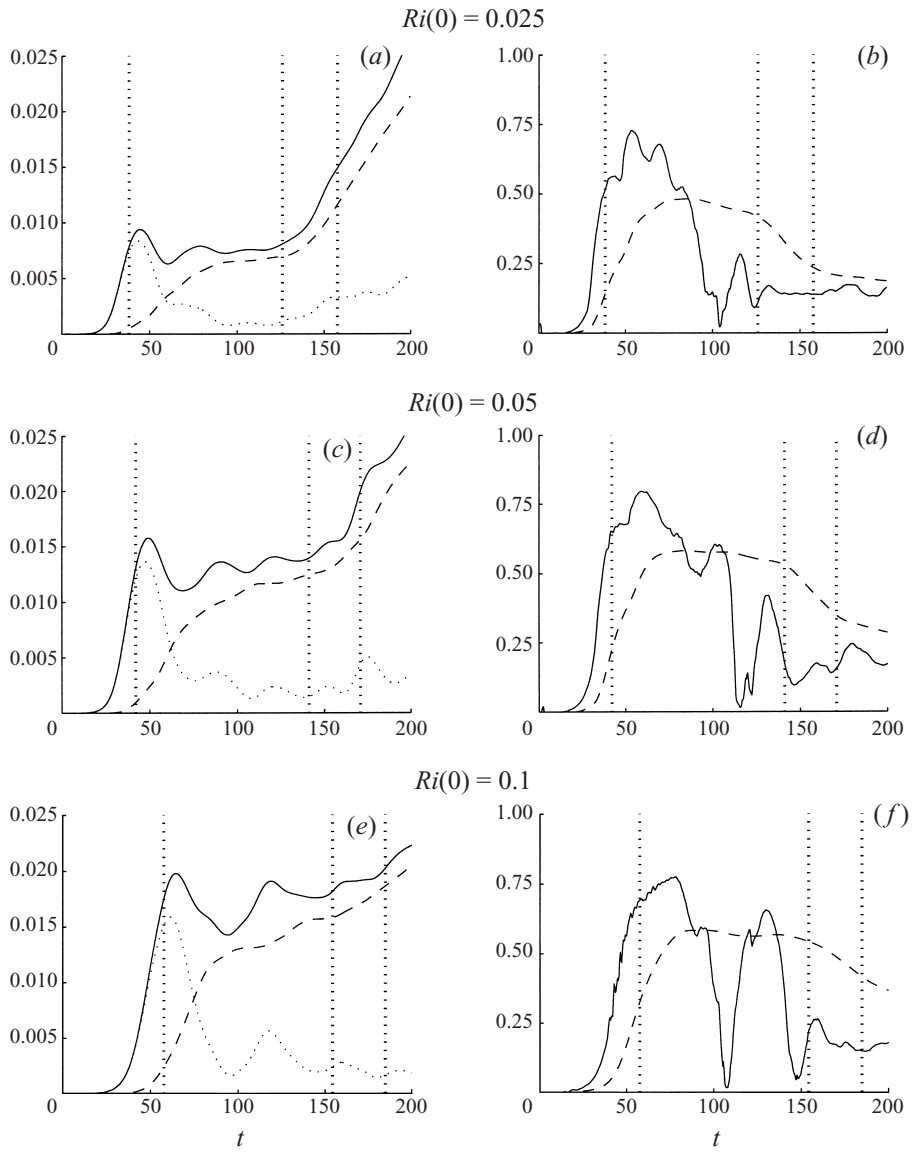

FIGURE 9. Time variation of $\mathscr{P}(t)-\mathscr{D}_{\mathscr{P}}t-\mathscr{P}(0)$ (defined by (2.27) and (2.29)) (solid line), $\mathscr{P}_A(t)-\mathscr{P}_A(0)$ (defined by (2.26)) (dotted) and $\mathscr{P}_B(t)-\mathscr{D}_{\mathscr{P}}t-\mathscr{P}_B(0)$ (defined by (2.25)) (dashed) for inherently three-dimensional simulations with (*a*) $Ri(0) = 0.025$; (*c*) 0.05; (*e*) 0.1, compared with the time variation of $\mathscr{E}_i$ (defined by (2.33)) (solid line) and $\mathscr{E}_c$ (defined by (2.34)) (dashed line) for inherently three-dimensional simulations with (*b*) $Ri(0) = 0.025$; (*d*) 0.05; (*f*) 0.1. The vertical dotted lines mark the characteristic times listed in figure 8.

decay (i.e. when $t_{3d\max} < t$), it is clear that $\mathscr{E}_c$ is still decreasing in this final stage of flow evolution, with a time variation which has changed qualitatively from that observed during transition. It is also apparent that the oscillations (associated with the re-development of statically unstable regions) in $\mathscr{E}_i$ observed in inherently two-dimensional simulations (cf. figure 5) do not occur in three-dimensional flows to anywhere near the same extent. This is due to the destruction of the primary billow core at late times in three-dimensional flows.

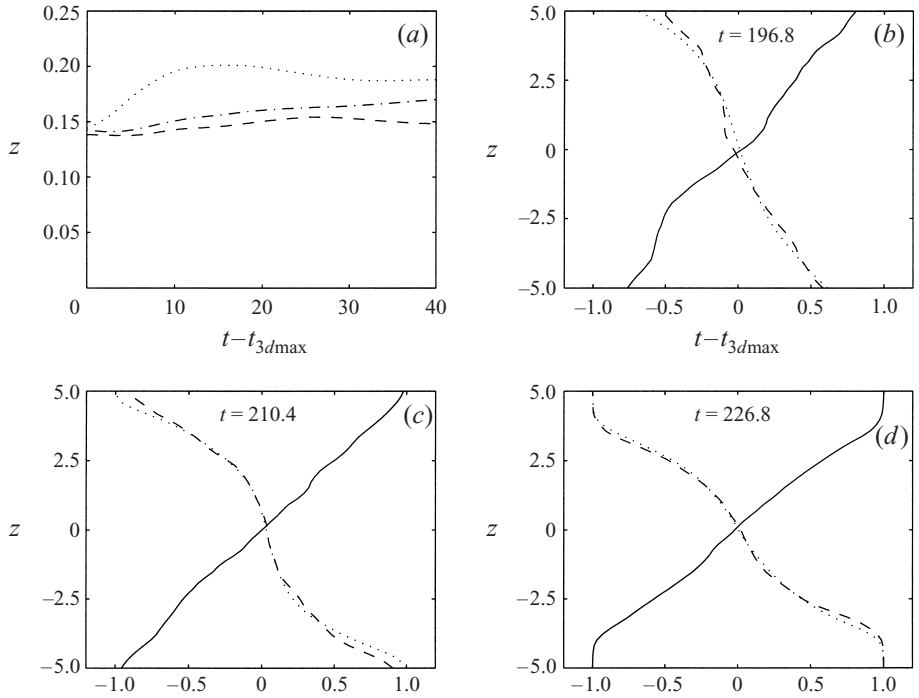

FIGURE 10. (*a*) Variation of the post-transition cumulative mixing efficiency ($\mathscr{E}_c^t$ defined by (5.1)) with $t - t_{3d\,\max}$ (listed in figure 8) for inherently three-dimensional simulations with $Ri(0) = 0.025$ (dashed line), 0.05 (dotted) and 0.1 (dot-dashed). (*b–d*) Vertical profiles of: $\bar{V}(z)$ (defined by (2.8)) (solid line), $\bar{\rho}(z)$ (defined by (2.12)) (dashed), and $\rho_B(z)$ (defined by (2.25)) (dotted) at time $t - t_{3d\,\max} = 40$ (listed in figure 8), for three-dimensional flows with (*b*) $Ri(0) = 0.025$; (*c*) 0.05; (*d*) 0.1.

Since we wish to draw comparisons with experimental calculations of a mixing efficiency within (forced) flows with significant levels of turbulence, it is perhaps more appropriate to attempt to consider a mixing efficiency of the flow when it is inherently three-dimensional. Furthermore, the dissipation within the flow during the KH billow roll-up and the (initial) development of the three-dimensional motions is so small that it is not really an appropriate analogue of the work done on a fluid by, for example, a stirring rod (see e.g. Park *et al.* 1994). However, if the normalized dissipation rate $\mathscr{D}$ has increased significantly after transition there is a plausible analogy between the work done by a stirring rod (causing small-scale motions which both mix the fluid and also suffer enhanced dissipation) and the energy lost by the total flow to mixing and dissipation. Therefore, we define a post-transition (cumulative) mixing efficiency as

$$\mathscr{E}_c^t(t - t_{3d\,\max}) \equiv \frac{\displaystyle\int_{t_{3d\,\max}}^{t} \mathscr{M}(u)\,\mathrm{d}u}{\displaystyle\int_{t_{3d\,\max}}^{t} \mathscr{M}(u)\,\mathrm{d}u - \int_{t_{3d\,\max}}^{t} \mathscr{D}(u)\,\mathrm{d}u}, \tag{5.1}$$

which essentially isolates the efficiency of the mixing during the fourth and final stage of the flow evolution when $t > t_{3d\,\max}$.

We plot this quantity in figure 10(*a*) against time for the three stratified calculations during the final stage of three-dimensional perturbation decay. Ultimately, in a

real flow the perturbations will decay, and the flow will return to laminar motion. Since there is significantly enhanced dissipation (and to a lesser extent mixing) during the post-transition phase of the flow evolution, the (total) cumulative mixing efficiency $\mathscr{E}_c$ will be dominated by contributions from this phase, and so $\mathscr{E}_c \sim \mathscr{E}_c^t$. The post-transition cumulative mixing efficiency thus serves as a useful estimate for the asymptotic value of the mixing efficiency. We choose the time $t_{3d\,\max}$ as a natural start time for the calculation of the post-transition mixing efficiency in (5.1). Variation in the start time naturally varies the numerical value of $\mathscr{E}_c^t$ somewhat, but not significantly provided the start time is chosen a sufficiently long time after transition so that the flow is dominated by small-scale disordered motions.

Using this method to filter out the contributions to mixing of the flow during periods of approximately laminar motion, we see that the typical (cumulative) mixing efficiency rates are of the order of 0.15, very much in line with the experimental evidence (Thorpe 1973; Linden 1979). Furthermore, when mixing during periods of intense, disordered motion is considered alone, there appears to be a non-monotinicity in the calculated cumulative and instantaneous mixing efficiencies, the mixing within the $Ri(0) = 0.05$ flow being the most efficient of the three flows which we have considered. This flow is still susceptible to relatively intense transient mixing events, whereas both the other stratified simulations are not. For the $Ri(0) = 0.025$ flow, variations in the density field are small after transition so that the disordered motion is unable to generate significant quantities of irreversible mixing, while the dissipation within the flow is very large, and so the mixing efficiency is small. Conversely, for the more strongly stratified $Ri(0) = 0.1$ flow, the ambient stratification suppresses mixing strongly at the periphery of the mixing layer, where the disordered motions are also less energetic.

Such non-monotonicity has been proposed on theoretical grounds (see Phillips 1972 and Posmentier 1977) to be the generic behaviour of mixing induced by small-scale turbulent motions in a stratified fluid, and been widely studied both theoretically (Barenblatt 1993; Balmforth *et al.* 1998) and experimentally (Linden 1979; Fernando 1991; Park *et al.* 1994). A particular aspect of flows with such non-monotonicity of mixing efficiency is that they are expected to become layered, with relatively weakly stratified layers of well-mixed fluid being separated by thin regions of high density gradient, a circumstance which is commonly encountered in nature, particularly in the upper reaches of the ocean (see Phillips 1972; Woods 1968). Our calculations appear to suggest that the mixing induced by the collapse of an unforced three-dimensional shear layer has mixing efficiency (when appropriately defined) comparable to the mixing efficiency found in forced flows. Furthermore, the dependence of the mixing efficiency on $Ri(0)$ appears to verify that shear-induced turbulent transition is a plausible mechanism, of itself, for the creation of a layered density field. This is particularly interesting, as the characteristics of the shear layer flow are qualitatively different from the flows previously considered. In particular, there is not a strong scale separation between the characteristic turbulence scales and the characteristic scale of the density gradient in the shear layers we are considering.

To investigate whether the density field is actually becoming layered within the stratified flows which we have considered, in figure 10(*b–d*), we plot the mean velocity profile $\bar{V}(z)$ (as defined in (2.8)), the mean density profile $\bar{\rho}(z)$ (as defined in (2.12)), and the background density profile $\rho_B(z)$ (as implicitly defined in (2.25)) at the last time shown in figure 10(*a*), i.e. at $t_{3d\,\max} + 40$. In each simulation the primary KH billow has been completely destroyed. There is some slight variation between $\bar{\rho}$ and ρ_B implying somewhat stronger density gradients at the edges of the mixed regions

within the flow. The depth of the mixed region within the flow decreases as $Ri(0)$ increases, but it is apparent that the characteristic scale over which the background density field varies has increased to at least five shear layer half-depths. At this late stage the primary billow cores are destroyed, and the characteristic scales of the fluid motion are naturally significantly smaller (typically of the order of the shear layer half-depth, as we show in the next section). Therefore, at this late stage of the flow evolution, it appears that, consistently with the models discussed by Linden (1979), the scales of turbulence are small compared with the regions of density gradient, and thus the ultimate development of a layered density profile may possibly be expected. The background velocity profiles are relatively smooth, and they all show a significant deceleration due to dissipation.

The qualitative character of the density profiles is also different. For the flow with $Ri(0) = 0.025$, the density distribution has become approximately linearly stratified throughout much of the flow domain. At the instant shown, the small-scale motions are still highly energetic, and it is reasonable to suppose that mixing will continue for a significant time subsequently, leading to an essentially complete mixing of the fluid density. Conversely, for the flow with $Ri(0) = 0.1$, the density stratification is too strong for the small-scale motions to erode it completely, and thus the region of the flow where mixing has taken place is still quite strongly stratified. However, there is a vertical variation in the density gradient, with the middle of the flow (where the small-scale motions have been most intense) more weakly stratified than other regions of the flow. This effect is more pronounced in the intermediate flow (with $Ri(0) = 0.05$) with a discernible well-mixed region developing in the central region, bounded by two thinner regions of stronger density gradient. Therefore, shear-induced three-dimensional mixing with intermediate stratification appears to lead to layering, while smooth density distributions appear to develop in both more weakly and more strongly stratified flows.

There is much greater variability throughout the entire flow evolution in the growth rate σ_{3d} of the inherently three-dimensional perturbation, as defined in (2.23), than the growth rates of the total kinetic energy of the flow and the spanwise-averaged perturbation kinetic energy, i.e. σ and σ_{kh} as defined in (2.20) and (4.4) respectively. In figure 11, we plot σ_{3d} and the various normalized contributions defined in (2.24) against time for each of the four different flows which we have considered. Also marked on the figure are the three special times defined in figure 8 which divide the four different stages of flow evolution (vertical dotted lines) and the theoretically predicted growth rates of three-dimensional perturbations (as in table 1) which we calculated in § 4.

In all cases, the perturbations experience growth which is rapid compared both to the rate of change of the two-dimensional perturbation field, and also the total flow, immediately upon saturation of the primary KH billow. This is an *a posteriori* verification that the assumption on which the stability analysis of § 4 was based is valid (i.e. a separation of timescales between the growth of three-dimensional perturbations and the timescale of variability of the two-dimensional flow). The continuous amplification of the three-dimensional perturbation (which remains highly organized) during this second stage of flow development strongly inhibits the onset of a tertiary instability since, in the absence of saturation, no timescale separation is possible. Significant dissipation accompanying the onset of small-scale disordered motion appears to occur during this period of strong three-dimensional perturbation growth.

The growth rates σ_{3d} exhibit significant oscillations in phase with the oscillations

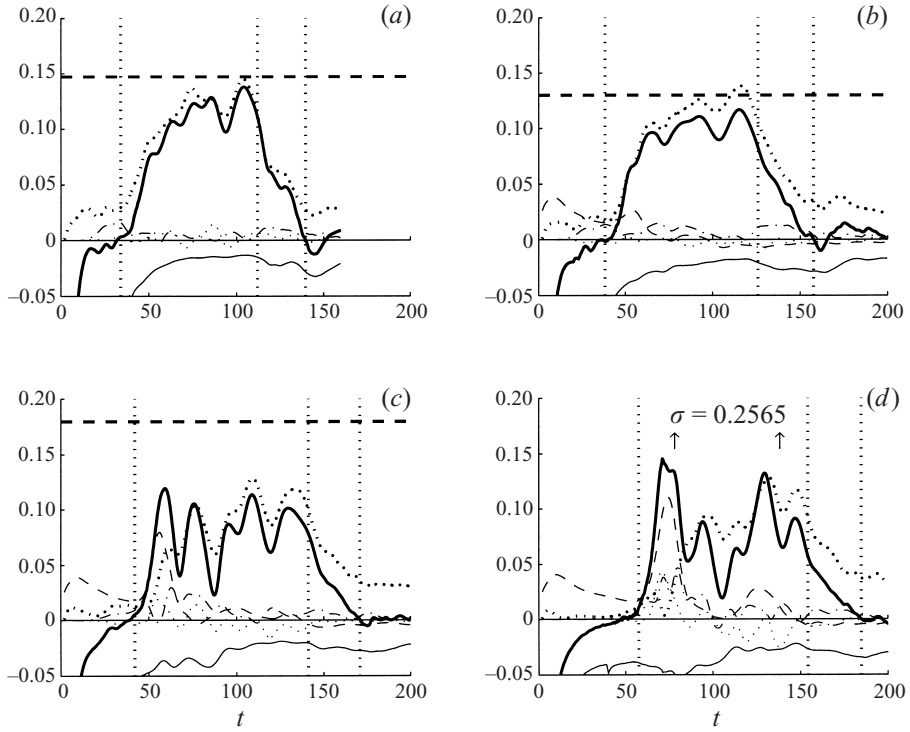

FIGURE 11. Time variation of σ_{3d} (defined in (2.23)) (solid thick line), $\hat{\mathscr{D}}_{3d}$ (solid thin), $\hat{\mathscr{H}}_{3d}$ (dashed), $\mathscr{S}\hat{\mathscr{H}}\mathscr{B}_{3d}$ (bold dotted), $\mathscr{S}\mathscr{H}\hat{\mathscr{K}}\mathscr{H}_{3d}$ (dotted), $\hat{\mathscr{S}}\mathscr{T}_{3d}$ (dot-dashed) (all defined in (2.24)), in inherently three-dimensional simulations with (*a*) $Ri(0) = 0$; (*b*) 0.025; (*c*) 0.05; (*d*) 0.1. Horizontal dashed lines mark the theoretical predictions listed in table 1.

of the background shear, indicative of reversible energy exchange between the background mean flow and the two-dimensional KH component of the flow. In all cases, periods of most rapid growth of the three-dimensional perturbations are associated with local temporal maxima in the background shear. Indeed, transition appears to occur immediately following one of these local maxima in growth rate, which occurs at the time t_f listed in figure 8.

For the unstratified flow in three dimensions, the dominant growth mechanism is through shear extraction from the background flow. For the flow with $Ri(0) = 0.025$, the shear contribution $\mathscr{S}\mathscr{H}\mathscr{B}_{3d}$ is still dominant, but at the moment of initial instability onset, there is a small positive contribution from the buoyancy flux term $\mathscr{H}_{3d}$. This transient peak is a signal of the exchange of some of the available potential energy $\mathscr{P}_A$ (stored in the statically unstable regions within the primary KH billow) back into kinetic energy of the total flow. The increase in kinetic energy is associated with a convective overturning which leads to some mixing, and hence an irreversible increase in $\mathscr{P}_B$, and it is this overturning motion which inevitably drives a three-dimensional perturbation. Once nucleated, this perturbation is then amplified further by the background flow. These post-saturation overturning and mixing events become increasingly significant as the Richardson number increases. For both of the more strongly stratified simulations, the initial growth of three-dimensional perturbations is dominated by a positive buoyancy flux contribution. Once the statically unstable regions have been eroded by both reversible and irreversible motions, the dominant

driving mechanism of the three-dimensional motions is through shear extraction $\mathscr{S}\mathscr{H}\mathscr{B}_{3d}$ from the mean shear.

Another effect of this initial intense buoyancy flux contribution is that the first local maximum in σ_{3d} varies non-monotonically with ambient stratification. Since this is a measure of the initial growth rate of very small three-dimensional disturbances, we consider this to be the appropriate analogue for the theoretically predicted growth rate of periodic small-amplitude perturbations which we calculated in § 4 (see table 1). The theoretical predictions in table 1 consistently overestimate the numerically inferred growth rate of the perturbations, due at least partly to the fact that the initial perturbations within our numerical simulations have not been tuned to the appropriate theoretical structures predicted in § 4.

This certainly seems to be the dominant effect for the unstratified and more weakly stratified simulations, in which the theoretically predicted growth rates overestimate the numerical observations by 10–15%. The behaviour of the two more strongly stratified simulations is qualitatively different, where the mismatch between observed and theoretically calculated growth rates is more severe, being of the order of 35% to 45%. The theoretical predictions are based on the assumption that the statically unstable regions at the periphery of the primary billow core are steady structures which do not evolve with time, which is clearly not the case. The initial convective overturning which triggers the onset of the three-dimensional perturbations also eliminates the dominant driving mechanism for these two simulations. Nevertheless, our numerical results remain qualitatively consistent with the theoretical predictions not only with regard to growth rate, but also concerning the variation of the relative significance of the various contributions ($\mathscr{S}\mathscr{H}\mathscr{B}_{3d}$, $\mathscr{H}_{3d}$ etc) with ambient stratification.

In figure 12, we plot σ_{3d} against time for each of the four simulations, with the different lines representing the parts of the relevant growth rate or contribution which are due to fluid motions in each of the four regions of interest (i.e. the 'core' region, the 'eyelid' region, the 'braid' region, and the remainder of the flow, as shown in figure 1). As usual, the vertical dotted lines denote the significant times shown in figure 8. The three regions of core, eyelid and braid contain virtually all of the fluid motions which are significant to three-dimensional perturbation growth. Considering the unstratified flow, this subdivision also enables us to determine conclusively the relative importance of core and braid-centred perturbations for the development of intense three-dimensional motions within the flow. From consideration of the plot of the subdivision of the growth rate σ_{3d} (figure 12*a*) the core region (dotted line) can be seen to be a region of very weak growth of three-dimensional perturbation throughout flow evolution. Substantial growth is predicted both in the braid, and in the eyelid region, though growth in the braid (solid thin line) appears to onset first, suggesting that perturbation growth in the braid region induces growth around the periphery of the primary billow core subsequently.

The three-dimensional motions are being driven in the braid region at all times in the flow evolution. This is entirely consistent with our theoretical prediction that, for an unstratified flow, the dominant mode of three-dimensional instability is the hyperbolic braid-centred instability first predicted in KP91. The onset of significant dissipation (an indicator of small-scale, disordered motion within the flow) occurs at a time when there is a final, very strong, and actually globally maximum peak in the growth rate of three-dimensional motions at the time t_f shown on figure 8, growth which is being driven almost exclusively by the shearing contribution from the background flow $\mathscr{S}\mathscr{H}\mathscr{B}_{3d}$. It appears that small-scale motions onset first within the braid region, and then spread throughout the flow, due to interac-

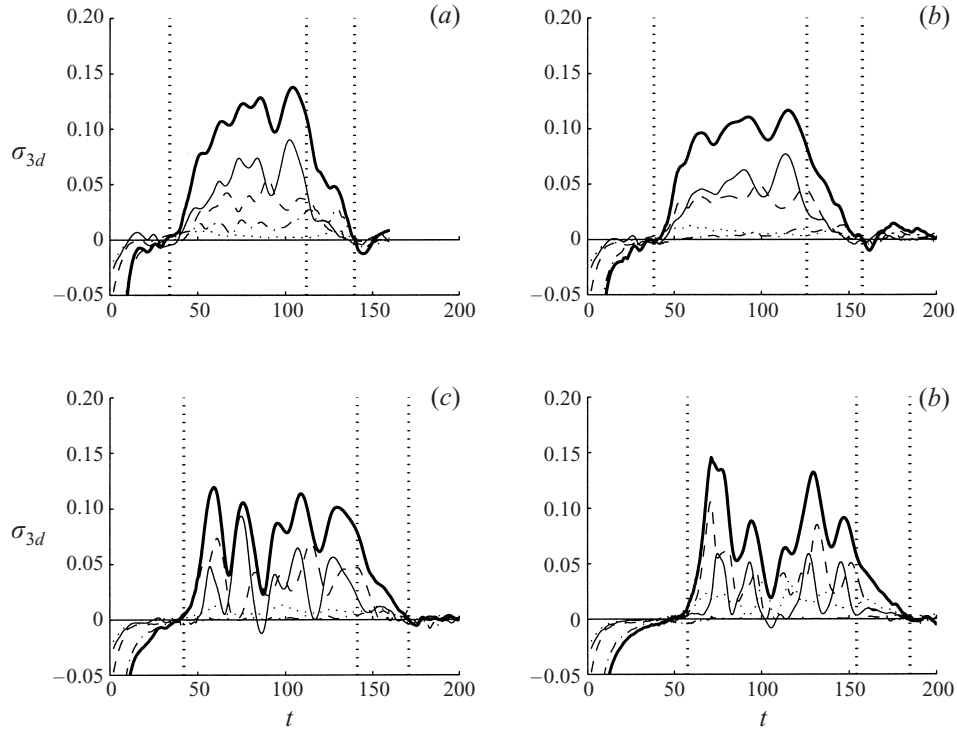

FIGURE 12. Time variation of total σ_{3d} (defined in (2.23)) (solid thick line) and the component associated with motions in the: braid region (solid thin); 'eyelid' region (dashed); core region (dotted), and the residual region (as defined in figure 1) (dot-dashed), for inherently three-dimensional simulations with (*a*) $Ri(0) = 0$; (*b*) 0.025; (*c*) 0.05; (*d*) 0.1.

tions between three-dimensional structures which initially develop in neighbouring braids.

The development of the weakly stratified flow with $Ri(0) = 0.025$ is similar in many respects to the development of the unstratified flow. Motions within the core (dotted lines) are largely insignificant in the flow evolution. By far the most significant growth mechanism is the shearing contribution from the braid region (thin solid lines). Transition onsets in the braid region, after a final, strong, globally maximum peak in the growth rate driven by a powerful shearing contribution. There is also significant growth in the 'eyelid' region (dashed lines) of the flow. There are also some differences, in particular the fact that the growth in the 'eyelid' region is briefly stronger than the growth in the braid region. This is caused by the buoyancy flux contribution $\mathscr{H}_{3d}$ (see figure 11*b*, dashed line) taking its only significant values right at the very beginning of flow development, and being initially concentrated in the eyelid.

As the ambient stratification is increased, the initial significance of $\mathscr{H}_{3d}$ in three-dimensional perturbation development increases markedly. In both of the more strongly stratified simulations, the buoyancy flux is the dominant initial contribution to the growth of three-dimensional perturbations. The first, and strongest, effect of the buoyancy flux contribution is felt in the eyelid region around the periphery of the primary KH billow core (dashed line), followed soon after by a contribution from the braid region (thin solid line). The further development of the perturbation is largely due to the shearing contribution $\mathscr{SHB}_{3d}$, with both the eyelid region and the braid

region playing significant roles. There is once again a strong signal (at time t_f) of shearing contribution in the braid region immediately prior to the onset of disordered motion with high dissipation rates. The initial stages of the development of three-dimensional perturbations in these direct numerical calculations for the more strongly stratified flows are also consistent with the predictions of the stability analyses of § 4. The perturbations are located initially in the eyelid region, and the buoyancy flux contribution is crucial to their initiation.

6. Spatial structure of three-dimensional motions

6.1. *Spanwise-averaged three-dimensional perturbation structure*

In figure 13, we plot the normalized spatial distribution of the spanwise average of the average three-dimensional perturbation kinetic energy at the time t_f (given in figure 8) $\bar{K}_{3d}(y, z, t_f)$, defined as

$$\bar{K}_{3d}(y, z, t_f) = \frac{\langle u_{3d}^2 + v_{3d}^2 + w_{3d}^2 \rangle_x}{2\mathscr{K}_{3d}(t_f)}. \tag{6.1}$$

The spatially varying quantity $\bar{K}_3 d$ is clearly the numerically simulated analogue of K_{3d} defined in (4.7) associated with a single secondary instability of the form given in (4.1). The qualitative similarity in the appearance of these figures and the theoretical predictions presented in § 4 (i.e. figure 7) is quite striking, particularly when it is remembered that figure 13 shows integrated representations of all the three-dimensional perturbations within the flow at a certain time, while figure 7 merely represents the eigenstructure of a single, monochromatic mode. In the unstratified simulation, the perturbation from early times is dominated by a braid-centred structure, which has developed in the hyperbolic region of the flow. At earlier times there is some evidence of a core-centred perturbation (highly similar to the low-wavenumber mode illustrated in figure 7(*a*) with a thick solid line) but there appears to be no communication between the braid-centred perturbation and the interior of the KH billow core, or indeed between neighbouring billows.

As has been the case with all the analyses which we have conducted, the behaviour of the flow with $Ri(0) = 0.025$ (figure 13*b*) has points of correspondence with both the stratified and unstratified flows. Initially, there is significant intensity in the braid region, but also a distinct double maximum in the perturbation kinetic energy at the leading edge below the primary billow core, and at the trailing edge above the primary billow core, exactly in the statically unstable regions induced by the roll-up of the primary KH billow. By the time t_f shown in the figure, the effect of background shear is to advect the three-dimensional perturbation into the braid region of the flow.

For the two more strongly stratified simulations, (i.e. figures 13*c* and 13*d*) we see that the major qualitative features of the predicted structure for the secondary instability are replicated in our simulations. The dominant contributions to the development of the three-dimensional perturbations in both flows are located around the periphery of the primary vortex core, with very little contribution from either the braid region or the interior of the primary billow core. There are clearly discernible peaks in $\bar{K}_{3d}$ for each of these simulations in the regions where the statically unstable convective regions have been induced, and furthermore, where the calculations of § 4 predict that the three-dimensional perturbations will be most intense.

We also find that although the initial mechanism and nucleation sites for the development of three-dimensional motions within shear layers strongly depend on the

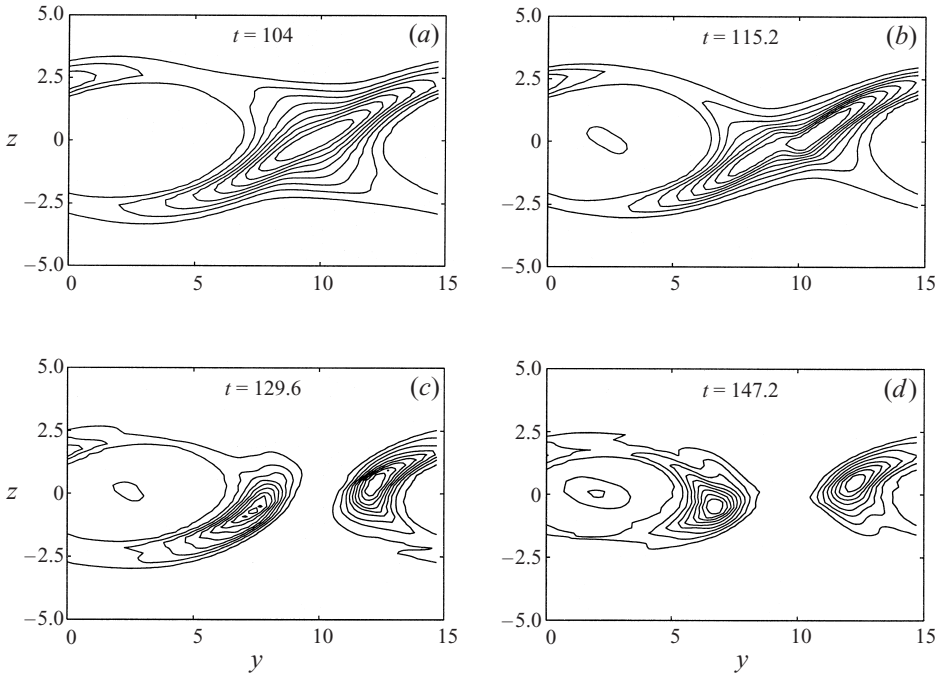

FIGURE 13. Spatial distribution of $\bar{K}_{3d}$ (defined in (6.1)) at the time t_f for inherently three-dimensional flows with (*a*) $Ri(0) = 0$; (*b*) 0.025; (*c*) 0.05; (*d*) 0.1.

ambient stratification, the mechanisms of nonlinear amplification of these structures and their ultimate destruction (thus precipitating the onset of transition) have certain aspects in common, irrespective of the ambient stratification. The braid region is the primary location for subsequent perturbation amplification. For the unstratified and most weakly stratified simulation ($Ri(0) = 0.025$) this is unsurprising, since the perturbation has initially developed in the braid, and so the perturbation extracts significant amounts of energy from the background flow via the shearing contribution $\mathscr{SHB}_{3d}$ and continues to amplify in its original region of development. The coherence of the primary billow core is quite remarkable, with the significant development of perturbations within the primary billow core being induced only when the three-dimensional perturbations become quite intense. This coherence of the primary billow core also implies that it is evolving rather similarly to the fashion in which it evolves when the flow is restricted to two dimensions, in particular that it is nutating and oscillating. This oscillation periodically intensifies the growth rate (and driving mechanism) of the three-dimensional perturbation at times when the background shear is most intense. Furthermore, as the primary billow rotates (in our figures always in a clockwise direction), the billow has the effect of further intensifying the three-dimensional perturbation structures by stretching and sweeping the perturbation over and under a primary billow core and towards a neighbouring braid. This injection and communication from one braid region to its neighbour is a fundamentally nonlinear process, which plays a significant role only subsequently to the appearance and development of the secondary instability.

Ultimately the perturbation reaches a critical amplitude. At the time t_f shown in the figures, there occurs a last local temporal maximum in background shear and hence σ_{3d}. At this instant, the process of injection of the perturbation from a neighbouring

braid region is so intense that small-scale motions rapidly develop, and then propagate throughout the flow field, with an attendant rapid increase in dissipation.

There is an analogous development of the flow in the more strongly stratified simulations. The perturbations have nucleated around the periphery of the primary billow core, principally at the trailing edge a little above the core, and also at the leading edge slightly below the core. Periodically with the oscillations of the primary billow core, these perturbations intensify and migrate towards the centre of the braid, as is indicated by the dominance of the shearing contribution from the braid region on their subsequent development. This migration of the perturbation towards the braid region oscillates in phase with the oscillation of the primary KH billow, until ultimately critical amplitude is reached around time t_f shown in the figure, and the two perturbations from neighbouring billows meet near the centre of the braid region (soon after the times t_f). This collision at finite amplitude triggers a rapid increase in dissipation and transition.

6.2. *Three-dimensional visualizations*

The streamwise vorticity is a highly appropriate field to consider if we wish to visualize the development of three-dimensional perturbations within a flow as it is inherently three-dimensional and the predicted secondary instabilities are characterized by spanwise-periodic streamwise vortices. In figures 14 and 15, we show isosurfaces of positive and negative streamwise vorticity at three different times. The times selected are during the second stage of flow development, when the three-dimensional perturbations are growing, essentially through energy extraction from the background flow. For ease of comparison between different simulations, the chosen times are defined for each of the flows which we are considering in terms of the differing values of the ratio $R_{\mathscr{K}}$, defined as

$$R_{\mathscr{K}} \equiv \mathscr{K}_{3d}/\mathscr{K}_{kh}. \tag{6.2}$$

The three values $R_{\mathscr{K}} = 3.3 \times 10^{-4}$, 1.0×10^{-2}, and 3.0×10^{-2}, are chosen to illustrate the development of three-dimensional perturbations within the second stage of the life cycle of the shear layer. We also show an isosurface of spanwise vorticity, which defines the extent of the 'core' region. We have varied the level of the vorticity isosurface between the different frames at different times so that it is possible to observe the underlying structure of the streamwise vortex tubes, which are amplifying significantly with time.

The three-dimensional structures which develop within shear layers may be thought of as streamwise vortex tubes. In the unstratified calculation, the tubes develop in the braid, while, as the stratification increases, the convectively unstable region at the trailing edge above the core and at the leading edge below the core become increasingly significant, with the most weakly stratified simulation exhibiting essentially hybrid behaviour. What is particularly striking about these figures is the high level of periodicity within the streamwise vorticity field in our calculations, which were forced in three dimensions purely with broadband white noise. Furthermore, the wavelength of the perturbations does not change noticeably with time within any one of the simulations, with no direct evidence of 'collapse' into isolated vortices, consistently with our theoretical predictions. Indeed, as $Ri(0)$ increases, there does seem to be a trend to smaller wavelength, as predicted in § 4.

The subcritical interaction between perturbations on neighbouring billows can be seen to be intimately related to a collision between the spanwise periodic array of streamwise-aligned vortex tubes. In the unstratified flow, a vortex tube (the finite-

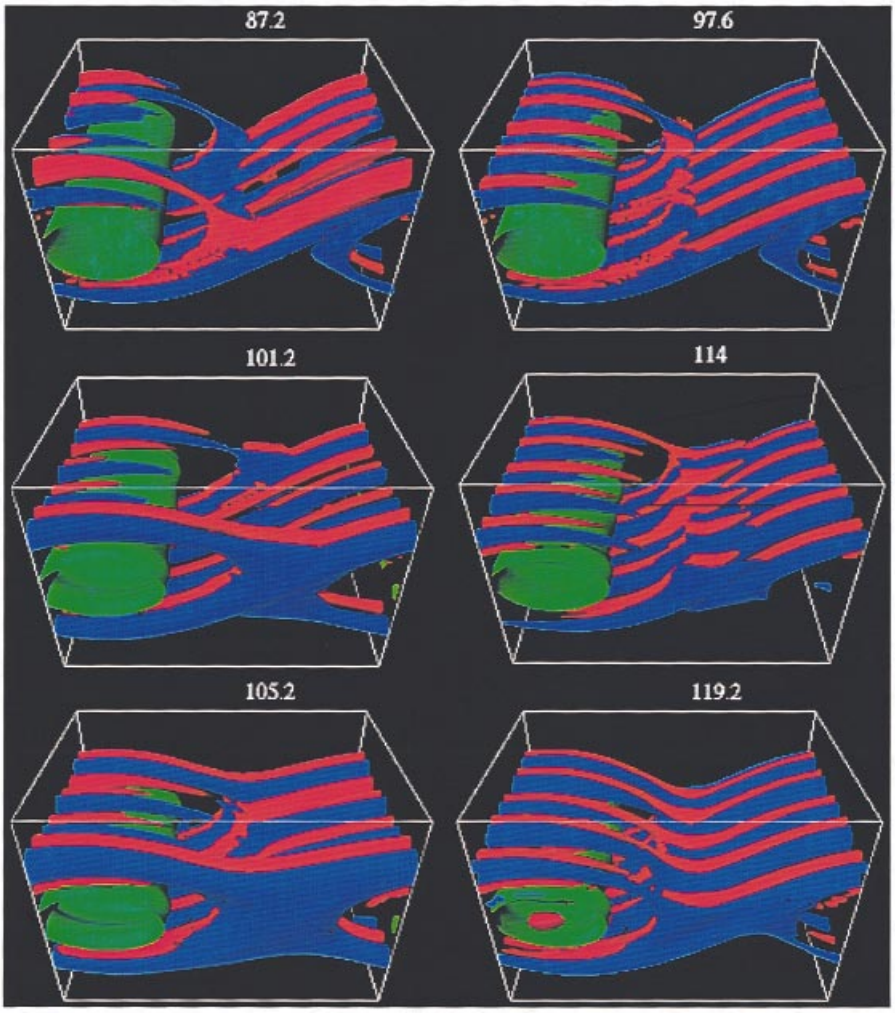

FIGURE 14. Isosurfaces of spanwise vorticity (green) with $\omega_x = -0.7$ and various isosurfaces of streamwise vorticity ω_y (positive blue and negative red) within an unstratified flow (left column) and a flow with $Ri(0) = 0.025$ (right column) at three different times as shown on the figure, defined in terms of the prevailing value of $R_{\mathscr{K}}$ (as defined in (6.2)): (*a*) $R_{\mathscr{K}} = 3.3 \times 10^{-4}$, $|\omega_y| = 0.02$; (*b*) $R_{\mathscr{K}} = 1.0 \times 10^{-2}$, $|\omega_y| = 0.1$; (*c*) $R_{\mathscr{K}} = 3.0 \times 10^{-2}$, $|\omega_y| = 0.1$.

amplitude manifestation of the hyperbolic instability) is intensified within the braid, and then starts to wrap around the primary KH billow core. It then passes into the flow field of the neighbouring braid, and is in turn intensified by the strain field associated with the neighbouring braid region. However, within this braid region, there is typically another, independently developing streamwise-aligned vortex tube. It is an interaction between these two neighbouring streamwise vortices which triggers the transition to turbulence.

At the early stages of the development of the three-dimensional motions, the intensity of the streamwise-aligned vortex tubes is relatively weak, and so the two neighbouring tubes do not interact particularly vigorously. When a weak streamwise vortex tube is swept round the primary KH billow into the vicinity of the neighbouring

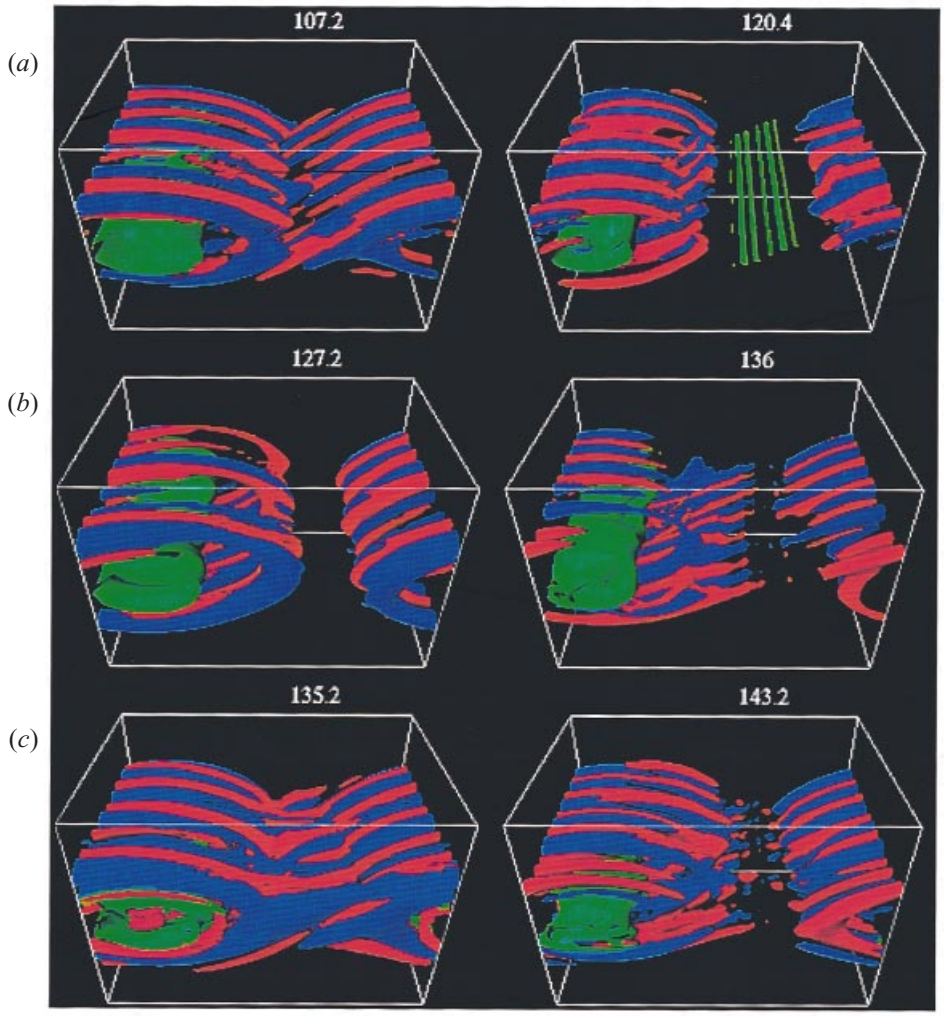

FIGURE 15. As figure 14 but with $Ri(0) = 0.05$ (left column) and $Ri(0) = 0.1$ (right column).

stagnation point, the flow field induced by the streamwise vortex tube which is actually developing at that stagnation point acts to deflect the approaching streamwise vortex tube away from the stagnation point. The incoming streamwise vortex tube is thus deflected onwards to the next primary KH billow core further downstream, where once again it continues to be amplified. This amplification is a continual process, principally driven by energy extraction from the background mean flow. The periodic exchange of energy between the mean flow, and the flow field associated with the primary KH billow core modulates the growth rate of the three-dimensional motions (cf. figure 11).

The background flow amplifies the streamwise-aligned vortex tubes until they attain a critical amplitude. This final surge in the growth in intensity of the streamwise vortex tube leads to a climactic interaction in the vicinity of the braid stagnation point. At this stage of the flow evolution, the streamwise vortex tube which is being swept inwards towards the stagnation point is sufficiently intense to break the local streamwise vortex tube which is continually being stretched at that particular

stagnation point. This finite-amplitude vortex–vortex interaction rapidly introduces small-scale, three-dimensional motions throughout the flow, and signifies the onset of disordered, turbulent motion.

The general structure of the transition to turbulence in a stratified flow is analogous to the unstratified flow. Transition appears to be mediated by intense, vortex–vortex interactions between the secondary streamwise-aligned vortex tubes, localized in the braid region of the flow. As can be seen clearly in figure 15, the streamwise vortices (in the various stratified flows which we have considered) develop initially around the periphery of the primary KH billow, at greatest amplitude below and slightly towards the leading edge of the billow core, and above and slightly towards the trailing edge of the billow core. Though initially triggered by convective overturnings within the statically unstable regions which develop around the periphery of the primary billow core, the careful analysis of the energetics of the flow which we presented in § 5 demonstrates that the subsequent development of three-dimensional motions to finite amplitude is due principally to shear extraction from the background flow.

The amplification of the three-dimensional motions by the background shear corresponds to a stretching of the secondary streamwise-aligned vortex tubes as can be seen in figure 15. The background shear causes these secondary vortex tubes to be stretched (and thus intensified) away from their initial nucleation sites around the periphery of the primary KH billow core. This stretching process advects the vortex tubes towards the braid region, and leads to the transient development of three-dimensional perturbations in the braid region.

Indeed, due to the particular structure of the flow field in the braid region, this stretching also causes the secondary streamwise-aligned vortex tubes, which have initially nucleated on neighbouring primary billow cores, to converge on the stagnation point at the middle of the braid region. Since there exists an underlying oscillation in the intensity of the background shear, this stretching process oscillates in intensity during growth of the three-dimensional motions.

As the three-dimensional motions develop, the background shear flow continues to stretch the streamwise vortex tubes (which originate from neighbouring primary KH billow cores) closer and closer towards the midpoint of the braid region. Eventually, at the time t_f when the background flow is most intense, the two neighbouring arrays of secondary streamwise-aligned vortex tubes are stretched sufficiently so that they collide near the middle of the braid region, as can be seen clearly in figure 15. Intense small-scale motions are induced within the flow as the colliding finite-amplitude streamwise vortex tubes (initially developed in the vicinity of neighbouring primary billow cores) interact. As they collide in the braid region, approaching each other in the streamwise direction, vigorous vortex reconnection processes occur which are inherently finite amplitude and subcritical. In all our simulations, there is little evidence of neighbouring streamwise vortices interacting strongly in the spanwise direction, and therefore, within the flows which we have considered, there appears to be no evidence of a tertiary instability of neighbouring counter-rotating vortex pairs, such as the so-called Crow instability (Crow 1970) or co-operative elliptical instabilities (see e.g. Leweke & Williamson 1998). It is important to appreciate that the flows which we have considered appear to undergo the transition to turbulence through a finite amplitude interaction of evolving secondary vortical structures which reconnect predominantly in the streamwise direction.

Such vortex reconnection is a possible explanation for the observation of tubes within tilted tank experiments (see Thorpe 1987 for a fuller discussion). Vortex tubes in the braid may develop from the three-dimensional perturbations initially localized

in the periphery of the primary vortex core. They are highly amplified compared to the initial instability structures, and may be experimentally observable, even if those shown in the frames of figure 15 are not. Due to the spanwise periodicity enforced by our chosen boundary conditions, and the two-dimensional form of our unstable mode initial perturbation, the initial primary billow cores are perfectly two-dimensional, and so there is initially no streamwise vorticity in the braid region. Nevertheless we do observe intense streamwise-aligned vortical structures in the braid region. In a less-constrained flow, if there is any element of non-parallel alignment in the primary billow cores (as experimentally observed by Thorpe 1987 and Caulfield *et al.* 1996, and deliberately induced by Atsavapranee & Gharib 1997) this will inevitably lead to streamwise vorticity being initially resident in the braid regions. The strain field in the braid region will naturally enhance this vorticity markedly, and thus contribute another, different mechanism for streamwise vortical development in the braid region, which is distinct from that considered in this paper, and theoretically predicted in § 4.

6.3. *Spectral representation*

It is sensible to attempt to compare quantitatively the spatial periodicity of the three-dimensional motions (clearly evident in figures 14 and 15) and the theoretical predictions of § 4. At each time step, we used fast Fourier transforms (in the spanwise direction) to obtain a discretized (spanwise) spectral representation of the streamwise vorticity field $\omega_y = \partial u/\partial z - \partial w/\partial x$. This representation took the form

$$\omega_y(x, y, z, t) = \sum_{n=-N}^{N} c_n(\gamma_n, y, z, t) \mathrm{e}^{\mathrm{i}\gamma_n x}. \tag{6.3}$$

The $c_n(\gamma_n, y, z, t)$ are the (complex) Fourier coefficients

$$c_n(\gamma_n, y, z, t) = \langle \omega_y \mathrm{e}^{-\mathrm{i}\gamma_n x} \rangle_x, \tag{6.4}$$

and the γ_n are a discrete set of spanwise wavenumbers $\gamma_n = n\gamma_1$, where $\gamma_1 = 2\pi/L_x$. For our calculations, the appropriate value of N was 64. Of natural interest is the relative importance of the various spectral components as represented by the normalized spanwise power spectrum density $P(\gamma_n)$ (for non-negative n) defined as

$$P(\gamma_n, t) \equiv \frac{\langle |c(\gamma_n, y, z, t)|^2 \rangle_{yz}}{\sum_{n=0}^{N} \langle |c(\gamma_n, y, z, t)|^2 \rangle_{yz}}. \tag{6.5}$$

We also compartmentalize the power spectrum density into parts associated with the billow core, 'eyelid' and braid, subdividing the flow in the same manner as was used for our energetics calculations, and as illustrated in figure 1.

In figure 16, we plot the (normalized) power spectrum density $P(\gamma_n, t)$ against γ_n at the time t_f (the same as used in figure 13) for each of the simulations which we are considering. In each plot, the various lines show the components of the power spectrum associated with motions in the different parts of the flow defined in figure 1.

For all the flows, the power spectrum has a strong peak at time t_f, which has developed from the initially broadband noise. When the flow is unstratified, for all times the peak appears to be concentrated in the braid region (thin solid line). Also significant is the 'eyelid' region around the periphery of the primary billow core (dashed line). Once again, the core region plays an insignificant role in the flow development. Since the flow was initially forced with a broadband spectrum of three-dimensional perturbations, it would appear that the most unstable perturbation

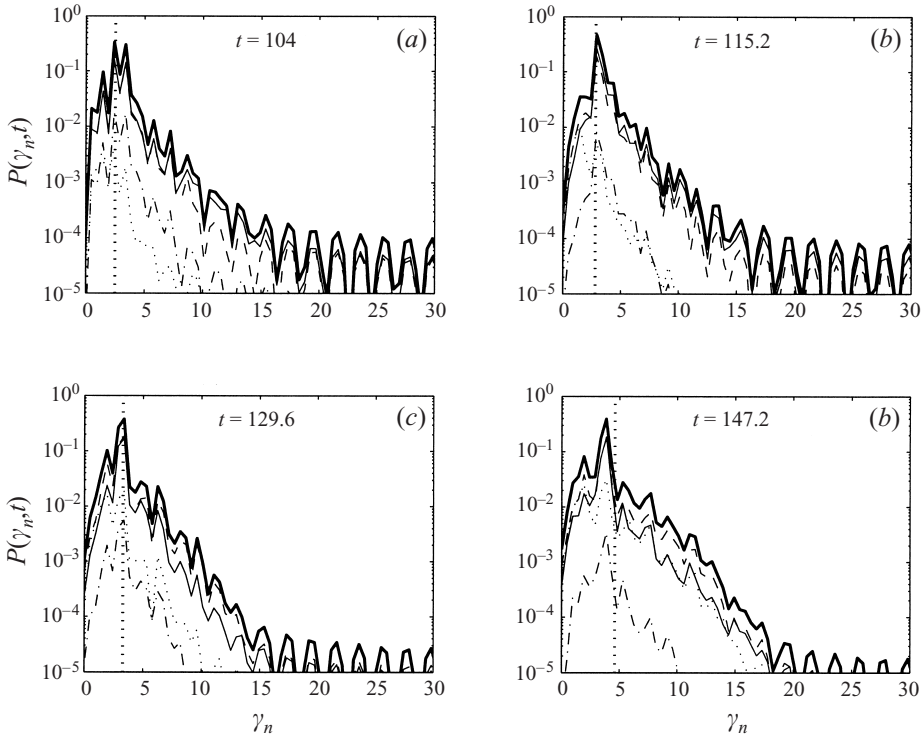

FIGURE 16. Variation of the various components (i.e. total (thick solid line), braid (thin solid), 'eyelid' (dashed), core (dotted) and remainder (dot-dashed) as defined in figure 1) of $\hat{P}(\gamma_n, t)$ (defined by (6.5)) against γ_n at the time t_f as defined in figure 8, for inherently three-dimensional flows with $Ri(0) =:$ (*a*) 0; (*b*) 0.025; (*c*) 0.05; (*d*) 0.1. The wavenumber of the most unstable mode predicted in §4 is denoted by a thick dotted line.

structure is dominating the later time development of the flow. This perturbation appears to be localized in the braid region of the flow.

The 'eyelid' region (plotted with a dashed line) around the periphery of the primary billow core becomes increasingly significant as the initial level of stratification is increased (figure 16*b–d*). When the flow is stratified, the precise timing of the development of the dominant peak in the power spectrum of the streamwise vorticity field appears to be directly after the initial peak in the buoyancy flux $\mathscr{H}_{3d}$, further support for our belief that the dominant secondary three-dimensional motions within the shear layer are initiated by a three-dimensional convective instability, localized around the periphery of the primary billow core, as theoretically discussed in §4. As three-dimensional motions develop within the flow, the power in the streamwise vorticity field localized in the braid region increases markedly (thin solid line), until at time t_f it typically is as significant as the eyelid region.

Importantly, until transition, it is possible to establish that there is a measurable continued reduction in the relative importance of higher wavenumber disturbances. From this evidence, it is reasonable to draw two inferences about the spatial periodicity of the streamwise vorticity field. First, as observed qualitatively by consideration of figures 14 and 15, the streamwise vorticity field organizes into a highly periodic array of streamwise-aligned vortices, whose characteristic periodicity does not vary appreciably with time. Secondly, these streamwise-aligned vortices do not appear to

collapse into highly isolated structures, as such a collapse would be associated with an increase in the relative significance of the higher wavenumber components of the flow field.

As the various flows further develop, the structure of the power spectrum of the streamwise vorticity field does not vary appreciably, although, due to the continual intensification of the three-dimensional motions, the total power in the streamwise vorticity field increases by several orders of magnitude. However, in each case, there is a quite abrupt change in the power spectrum immediately subsequent to the transition time t_d, the peak associated with the secondary streamwise vortices being rapidly eroded subsequently. A smooth power spectrum indicating a continual cascade to smaller scales develops.

In each of the figures we have marked the predicted value (from § 4) of the most unstable spanwise wavenumber for each of the particular flows with a thick vertical dotted line. The power spectra for the various flows show excellent quantitative agreement with the theoretical predictions, for all except the most strongly stratified simulation (with $Ri(0) = 0.1$, as plotted in figure 16(*d*), where the theoretical prediction is somewhat too large). As $Ri(0)$ is increased, the wavenumber associated with the peak in the power spectrum increases, in accord with our theoretical predictions.

7. Conclusions

We have analysed in detail four fully three-dimensional simulations of shear flows, with varying initial stratification. We have found that the life-cycle of a shear flow, from its initial laminar state to transition, is intimately related to the initial growth, development and ultimate breakdown of secondary, spanwise-periodic streamwise-aligned vortices. These vortices appear once the primary KH billow has saturated, and are naturally inherently three-dimensional. We have demonstrated, both qualitatively and quantitatively, that these streamwise vortex streaks may be considered to be finite-amplitude manifestations of secondary instabilities of the non-parallel flow induced by the roll-up of the primary billow core.

When the flow is unstratified, we show that the braid region is itself susceptible to a localized secondary instability, which we have referred to as a hyperbolic instability. If the braid region is subject to a spanwise-periodic perturbation, such a perturbation both naturally induces streamwise-aligned vorticity, and also is very efficient at extracting energy for further growth from the background shear flow. The appropriate perturbation takes the form of a translation of the braid region, thus leading to efficient energy extraction through Reynolds stresses by the perturbation from the background shear.

However, when the flow is stratified, the mechanisms of three-dimensionalization are fundamentally different. In such stratified flows, due to baroclinic effects, the vorticity of the braid is strongly intensified, thus modifying markedly the type of perturbation which can develop in this region. Also, since this region is also a region of intensified static stability, secondary vertical motions are strongly suppressed in the braid in general, thus suppressing the very type of motions which appear to be necessary for the development of the hyperbolic instability. The periphery of the primary KH billow is a location where the fluid is locally statically unstable, as the process of rolling up the spanwise vorticity has led to dense fluid being lifted up above light fluid. This process of redistribution of the density field causes the potential energy of the whole system to increase, but significantly, much of this increase in potential energy remains available to drive secondary motions. We show that the flow

is predicted to be linearly unstable to spanwise-periodic structures localized around the periphery (i.e. the 'eyelid') of the primary billow core.

This instability manifests itself physically as streamwise-aligned vortical motions, which are triggered by the release of the potential energy stored in the convectively unstable regions of the flow. Some of this released potential energy causes a burst of (irreversible) mixing around the periphery of the primary billow cores, which occurs soon after the saturation of the primary instability. However, some of the potential energy converts into kinetic energy, seeding a streamwise-aligned overturning, which is rapidly amplified by the background shear to finite amplitude, in the form of streamwise-aligned vortex tubes.

It is important to appreciate that the numerically observed spanwise wavenumbers in our three-dimensional simulations are largely in quantitative agreement with the theoretical calculations of § 4. The observed initial growth rates of the inherently three-dimensional motions are sufficiently large that there is a demonstrable separation of time scales between the evolution of the secondary perturbations and the spanwise-averaged two-dimensional flow. This separation of time-scales justifies *a posteriori* the underlying assumption of our analyses. In general, all the evidence of our studies points to the view that the non-parallel flow induced by the primary KH billow is, in a real sense, catalytic in the transition to turbulence, with the dominant growth mechanism for three-dimensional motions being direct energy extraction from the parallel, mean shear flow. During the three-dimensional simulations, the growth rate of the kinetic energy associated with the inherently three-dimensional motions oscillates strongly, with the maximum value being associated with periods of maximum ambient shear.

Furthermore, during this nonlinear amplification process, the various characteristics of the secondary perturbations do not vary significantly with time. In particular, there is no quantitative evidence of collapse' of the streamwise-aligned vortices into highly isolated vortices. The vortices actually appear to remain highly periodic, and essentially space-filling in the spanwise direction. Physically, the streamwise-aligned vortices are periodically stretched. In an unstratified flow, the main effect of this stretching is to advect a particular streamwise vortex towards the stagnation point at the midpoint of a braid region of a neighbouring billow. Analogously, for a stratified flow, stretching by the background shear causes the streamwise vortices (initially on the periphery of the primary billow core) to be advected towards the stagnation point at the midpoint of the braid region between neighbouring billows. In the stratified flows which we have considered, the density field appears to play no significant dynamic role during this phase of flow development. Also, during the intensification of the streamwise vortices, there is little mixing and an irreversible increase in the potential energy of the entire flow.

Ultimately, this intensification of the streamwise vortices leads to the onset of small-scale, disordered motion within the flow. The streamwise vortices become so intense that they interact subcritically with each other. This interaction takes the form of a streamwise-aligned collision in the vicinity of the stagnation point at the midpoint of the braid region. Though the particular route of approach to this collision varies with the ambient stratification (and hence the initial localization of the streamwise-aligned vortices) the onset of small-scale motions occurs first in the vicinity of the midpoint of the braid region.

These small-scale motions rapidly spread outwards from this point, as the streamwise-aligned vortices break down, destroying the primary billow core in the process. In general, there is a dramatic increase in the dissipation within the flow, over a

relatively short timescale. In the case of the stratified flows which we considered, this proliferation of inherently three-dimensional, small-scale motions also leads to a marked increase in the irreversible mixing within the flow. The spatial distribution of these small-scale motions is affected strongly by the ambient stratification. When the flow is unstratified the small-scale motions spread throughout the entirety of the flow domain, and the background shear profile is completely disrupted. When the flow is stratified, the large-scale stabilizing effects of the ambient density distribution causes the small-scale motions to be concentrated over a vertical extent of the order of the primary KH billow. Our observations suggest that the flow above and below the extent initially occupied by the primary KH billow remains essentially laminar.

Within the region of small-scale motion, though the appropriate Reynolds number within the flow is too small for the turbulence to become fully developed, the flow is eventually dominated by small-scale, slowly decaying, intense three-dimensional disordered motions. In the stratified flows, we observed intense, irreversible mixing occurring as the underlying disordered motions decayed. We have carefully analysed this mixing process, using the formalism proposed by Winters *et al.* (1995). By considering the developing background density distributions, we observed a non-monotonic dependence of an appropriate measure of the mixing efficiency on the initial ambient stratification.

Whatever the particular cause of and characteristics of the turbulent disordered motion, non-monotonic mixing efficiency as a function of ambient stratification implies the ultimate development of a layered density profile (Phillips 1972; Posmentier 1977; Linden 1979). Our analyses suggest that the small-scale motions induced by the development, intensification and ultimate breakdown of secondary, spanwise-periodic, streamwise-aligned vortices within a stratified shear flow drive mixing processes with this very non-monotonic mixing efficiency, at least over some (extended) period of time of flow evolution. Therefore, the mixing induced by flow breakdown within a stratified shear flow leads inevitably to a layered density profile. Indeed, the development of such layered profiles should be thought of as a generic final structure for turbulent mixing within stratified flows, irrespective of the particular characteristics of the three-dimensional mixing processes. Although we have not continued our simulations of the flows until the disordered motions decayed and the flows fully relaminarized, and thus could not verify the result directly, the evidence of the relatively early-time evolution of the mixing within the disordered flow is consistent with the ultimate development of a layered density profile (see figure 10).

To draw general conclusions from our study, the effects of the periodic boundary conditions in the spanwise and streamwise directions need to be carefully considered. In the spanwise direction, it is clear from figures 14 and 15 that the domain is sufficiently wide to allow the development of several streamwise-aligned vortices, and several different spanwise periodicities can be accommodated within the finite domain width. Also, the domain is sufficiently wide to accommodate elliptical instabilities of typical, theoretically predicted wavenumber, although our studies confirm that such instabilities play an insignificant role. Actually, the imposition of spanwise periodicity is of greater significance earlier in the flow evolution, as the periodicity encourages the development of a perfectly two-dimensional primary billow core. Though, from the experimental evidence, such a two-dimensional billow is often observed, the initial instability of a real shear flow can also often be inherently three-dimensional. The primary array of billows may not all be precisely perpendicular to the background flow, and the billows which develop may be of a finite horizontal extent, with complex patterns of defects and vortex reconnections (see Browand & Prost-Domasky 1990).

It is important to consider the effect of the imposition of periodicity in the streamwise direction, which essentially restricts our investigations to the evolution of the local flow around a single billow. Through our study, we have found that intense mixing may onset exclusively due to local motions induced in the vicinity of a primary KH billow, where the secondary, quasi-two-dimensional vortex merging instability has been artificially suppressed due to the imposition of streamwise periodicity, on the typical length scale of one KH billow. To demonstrate that the behaviour of the flows which we have considered is relevant to the development of flows with significantly greater streamwise extent, it is necessary to relax somewhat the imposition of periodicity in the streamwise direction. A natural extension is to define the streamwise extent of the flow so that two KH billows are able to develop within the computational domain. In such a flow, there is now a competition between two different routes to significant mixing, as considered in some detail in the context of unstratified flows by Rogers & Moser (1992). Locally to each billow, the three-dimensional instabilities which we have discussed in this paper grow simultaneously with the development of a largely two-dimensional secondary subharmonic merging instability. The exact route to intense mixing depends in a subtle manner on the initial amplitude of the various perturbations.

Unless the subharmonic forcing is sufficiently large that neighbouring primary KH billows merge relatively quickly, the three-dimensional perturbations develop, intensify, and trigger transition without any significant interaction between the neighbouring spanwise structures. As we have previously reported (Caulfield & Peltier 1994), the three-dimensional development of a stratified shear layer within a streamwise-periodic domain containing two primary KH billows can also exhibit the development of intense, spanwise-periodic streamwise-aligned vortices, which trigger the transition to turbulence. If the subharmonic forcing is sufficiently weak, we have found that stratified (and also unstratified) flows become intensely disordered before any significant interaction between the two primary billows takes place, thus confirming that, at least under certain circumstances, it is appropriate to consider the development of a flow consisting of a single KH billow as typical of the three-dimensional development and ultimate breakdown of an initially parallel shear flow.

Secondary stability analysis of the primary KH billow is highly valuable in identifying the characteristic secondary instabilities which develop. The secondary instability which appears to dominate in an unstratified flow is, as originally discussed in KP91, inherently localized in the hyperbolic, braid region of the flow, and though translative in nature, does not appear to be related to the elliptical instability of the primary billow core. Within stratified flows, the secondary instability spectrum is dominated by a convective instability, as first hypothesized in Peltier *et al.* (1978) and analysed in detail in KP85, that is localized in the statically unstable regions around the periphery of the primary billow core.

At finite amplitude, both types of instability take the form of streamwise-aligned vortices. These vortices grow inexorably through direct energy transfer from the mean flow. They do not, in the conventional sense, appear to undergo a tertiary instability, as within the flows which we studied the amplitude of the secondary, inherently three-dimensional motions never appeared to saturate until after the onset of small-scale disordered motions. Rather, flow breakdown is induced by a catastrophic subcritical interaction of streamwise-aligned vortices which have initially nucleated in the vicinity of neighbouring KH billow cores, which leads rapidly to highly disordered motions.

The ultimate interest in our study of stratified flows is the (irreversible) mixing induced by the disordered motions arising from the breakdown of the various primary

and secondary instabilities inherent in a temporally evolving stratified shear flow. From a quantitative analysis of the mixing efficiencies of such flows, the evidence appears to point to the inevitable development of layered density distributions, after the turbulence has decayed. Therefore, we conjecture that shear layer transition, in and of itself, is a possible mechanism for the development of multiple layers of different density within an initially essentially two-layer fluid. We will investigate the late-time development of such shear layers in a subsequent publication.

This research has been supported at the University of Toronto by Research Grant A9627 from the Natural Sciences and Engineering Research Council of Canada and by awards of time on the Cray C90 computer that is operated by Cray Research Inc. C.P.C. also acknowledges the support of the Royal Society and the Nuffield Foundation.

REFERENCES

Ashurst, W. T. & Meiburg, E. 1988 Three-dimensional shear layers via vortex dynamics. *J. Fluid Mech.* **189**, 87–116.

Atsavapranee, P. & Gharib, M. 1997 Structures in stratified plane mixing layers and the effects of cross-shear. *J. Fluid Mech.* **342**, 53–87.

Balmforth, N. J., Llewellyn Smith, S. G. & Young, W. R. 1998 Dynamics of interfaces and layers in a stratified turbulent fluid. *J. Fluid Mech.* **355**, 329–358.

Barenblatt, G. I., Bertsch, M., Dal Paso, R., Prostokishin, V. M. & Ughi, M. 1993 A mathematical model of turbulent heat and mass transfer in stably stratified shear flow. *J. Fluid Mech.* **253**, 341–358.

Bayly, B. J. 1986 Three-dimensional instability of elliptical flow. *Phys. Rev. Lett.* **57**, 2160–2163.

Bayly, B. J., Orszag, S. A. & Herbert, T. 1988 Instability mechanisms in shear flow transition. *Annu. Rev. Fluid Mech.* **20**, 359–391.

Bender, C. M. & Orszag, S. A. 1978 *Advanced Mathematical Methods for Scientists and Engineers.* McGraw-Hill.

Bernal, L. P. & Roshko, A. 1986 Streamwise vortex structure in plane mixing layers. *J. Fluid Mech.* **170**, 499–525.

Browand, F. K. & Prost-Domasky, S. 1990 Experiment on pattern evolution in the two-dimensional mixing layer. In *New Trends in Nonlinear Dynamics and Patterning Phenomena: The Geometry of Non-Equilibrium* (ed. P. Coullet & P. Huerre). Plenum.

Brown, G. L. & Roshko, A. 1974 On density effects and large structure in turbulent mixing layers. *J. Fluid Mech.* **64**, 775–816.

Cambon, C., Teissèdre, C. & Jeandal, D. 1985 Études d'effets couplés de déformation et de rotation sur une turbulence homogène. *J. Méc. Théor. Appl.* **4**, 629–657.

Caulfield, C. P. & Peltier W. R. 1994 Three-dimensionalization of the stratified mixing layer. *Phys. Fluids.* **6**, 3803–3805.

Caulfield, C. P., Yoshida, S. & Peltier, W. R. 1996 Secondary instability and three-dimensionalization in a laboratory accelerating shear layer. *Dyn. Atmos. Oceans* **23**, 125–138.

Clark, T. L. 1977 A small-scale dynamic model using a terrrain-following coordinate transformation. *J. Comput. Phys.* **24**, 186–215.

Clever, R. M. & Busse, F. H. 1991 Three-dimensional convection in a horizontal fluid layer subjected to a constant shear. *J. Fluid Mech.* **234**, 511–527.

Corcos, G. M. & Lin, S. J. 1984 The mixing layer: deterministic models of turbulent flow: Part 2. The origin of the three-dimensional motion. *J. Fluid Mech.* **139**, 67–95.

Corcos, G. M. & Sherman, F. S. 1984 The mixing layer: deterministic models of turbulent flow: Part 1. Introduction and the two-dimensional flow. *J. Fluid Mech.* **139**, 29–65.

Cortesi, A., Yadigaroglau, G. & Bannerjee, S. 1998 Numerical investigation of the formation of three-dimensional structures in stably-stratified mixing layers. *Phys. Fluids* **10**, 1449–1473.

Crow, S. C. 1970 Stability theory for a pair of trailing vortices. *AIAA J.* **8**, 2172.

Davis, P. A. & Peltier, W. R. 1979 Some characteristics of the Kelvin–Helmholtz and resonant

over-reflection modes of shear flow instability and of their interaction through vortex pairing. *J. Atmos. Sci.* **36**, 2394–2412.

Domaradzki, J. A. & Metcalfe, R. W. 1988 Direct numerical simulations of the effects of shear on turbulent Rayleigh-Bérnard convection. *J. Fluid Mech.* **193**, 499–531.

Drazin, P. G. & Reid, W. H. 1981 *Hydrodynamic Stability*. Cambridge University Press.

Fernando, H. J. S. 1991 Turbulent mixing in stratified fluids. *Ann. Rev. Fluid Mech.* **23**, 455–493.

Gallagher, A. P. & Mercer, A. McD. 1965 On the behaviour of small disturbances in plane Couette flow with a temperature gradient. *Proc. R. Soc. Lond.* A **286**, 117–1128.

Herbert, T. 1988 Secondary instability mechanisms of boundary layers. *Ann. Rev. Fluid Mech.* **20**, 487–526.

Howard, L. N. 1961 Note on a paper of John W. Miles. *J. Fluid Mech.* **10**, 509–512.

Hussain, A. K. M. F. 1983 *Turbulence & Chaotic Phenomena in Fluids* (ed. T. Tatsumi), pp. 453–460. North-Holland.

Kelly, R. E. 1967 On the stability of an inviscid shear layer which is periodic in space and time. *J. Fluid Mech.* **27**, 657–689.

Klaassen, G. P. & Peltier, W. R. 1985*a* The onset of turbulence in finite amplitude Kelvin–Helmholtz billows. *J. Fluid Mech.* **155**, 1–35 (referred to herein as KP85).

Klaassen, G. P. & Peltier, W. R. 1985*b* The effect of Prandtl number on the evolution and stability of Kelvin–Helmholtz billows. *Geophys. Astrophys. Fluid Dyn.* **32**, 23–60.

Klaassen, G. P. & Peltier, W. R. 1989 The role of transverse secondary instabilities in the evolution of free shear layers. *J. Fluid Mech.* **202**, 367–402.

Klaassen, G. P. & Peltier, W. R. 1991 The influence of stratification on secondary instabilities in free shear layers. *J. Fluid Mech.* **227**, 71–106 (referred to herein as KP91).

Knio, O. M. & Ghoniem, A. F. 1992 The three-dimensional structure of periodic vorticity layers under non-symmetric conditions. *J. Fluid Mech.* **243**, 353–392.

Koop, G. & Browand, F. K. 1979 Instability and turbulence in stratified fluids. *J. Fluid Mech.* **93**, 135–159.

Landman, M. J. & Saffman, P. G. 1987 Three-dimensional instability of strained vortices in a viscous fluid. *Phys. Fluids* **30**, 2339–2342.

Lasheras, J. C., Cho, J. S. & Maxworthy, T. 1986 On the origin and evolution of streamwise vortices in a plane free shear layer. *J. Fluid Mech.* **172**, 231–258.

Lasheras, J. C. & Choi, H. 1988 Three-dimensional instability of a plane shear layer: an experimental study of the formation and evolution of streamwise vortices. *J. Fluid Mech.* **189**, 53–86.

Lawrence, G. A., Browand, F. K. & Redekopp, L. G. 1991 The stability of a sheared density interface. *Phys. Fluids* A **3**, 2360–2370.

Lesieur, M., Comte, P. & Métais, O. 1995 Numerical simulations of coherent vortices in turbulence. *Appl. Mech. Rev.* **48**, 121–149.

Leweke, T. & Williamson, C. H. K. 1998 Cooperative elliptic instability of a vortex pair. *J. Fluid Mech.* **360**, 85–119.

Lin, S. J. & Corcos, G. M. 1984 The mixing layer: deterministic models of turbulent flow: Part 3. The effect of plane strain on the dynamics of streamwise vortices. *J. Fluid Mech.* **141**, 139–178.

Linden, P. F. 1979 Mixing in stratified fluids. *Geophys. Astrophys. Fluid Dyn.* **13**, 2–23.

Lorenz, E. N. 1955 Available potential energy and the maintenance of the general circulation. *Tellus* **7**, 157–167.

Metcalfe, R. W., Orszag, S. A., Brachet, M. E., Menon, S. & Riley, J. 1987 Secondary instability of a temporally growing mixing layer. *J. Fluid Mech.* **184**, 207–243.

Miles, J. W. 1961 On the stability of heterogeneous shear flows. *J. Fluid Mech.* **10**, 496–508.

Moser, R. D. & Rogers, M. M. 1993 The three-dimensional evolution of a plane mixing layer: pairing and transition to turbulence. *J. Fluid Mech.* **247**, 275–320.

Nygaard, K. J. & Glezer, A. 1990 Core instability of the spanwise vortices in a plane mixing layer. *Phys. Fluids.* A **2**, 461–464.

Nygaard, K. J. & Glezer, A. 1991 Evolution of streamwise vortices and generation of small-scale motion in a plane mixing layer. *J. Fluid Mech.* **231**, 257–301.

Nygaard, K. J. & Glezer, A. 1994 The effect of phase variations and cross-shear on vortical structures in a plane mixing layer. *J. Fluid Mech.* **276**, 21–59.

Orszag, S. A. & Patera, A. T. 1983 Secondary instability of wall bounded shear flows. *J. Fluid Mech.* **128**, 347–385.

Palmer, T., Fritts, D. & Andreassen, O. 1996 Evolution and breakdown of Kelvin–Helmholtz billows in stratified compressible flows. Part 2: Instability structure, evolution and energetics. *J. Atmos. Sci.* **53**, 3192–3212.

Park, Y. G., Whitehead, J. A. & Gnanadeskian, A. 1994 Turbulent mixing in stratified fluids, layer formation and energetics. *J. Fluid Mech.* **279**, 279–312.

Peltier, W. R., Hallé J. & Clark, T. L. 1978 The evolution of finite-amplitude Kelvin–Helmholtz billows. *Geophys. Astrophys. Fluid Dyn.* **10**, 53–87.

Phillips, O. M. 1972 Turbulence in a strongly stratified fluid is unstable? *Deep-Sea Res.* **19**, 79–81.

Pierrehumbert, R. T. 1986 Universal short wave instability of two-dimensional eddies in an inviscid fluid. *Phys. Rev. Lett.* **57**, 2157–2159.

Pierrehumbert, R. T. & Widnall, S. E. 1982 The two- and three-dimensional instabilities of a spatially periodic shear layer. *J. Fluid Mech.* **114**, 59–82.

Posmentier, E. S. 1977 The generation of salinity fine structures by vertical diffusion. *J. Phys. Oceanogr.* **7**, 298–300.

Potylitsin, P. G. & Peltier, W. R. 1998 Stratification effects on the stability of columnar vortices on the f-plane. *J. Fluid Mech.* **355**, 45–79.

Rogers, M. M. & Moser, R. D. 1992 The three-dimensional evolution of a plane mixing layer: the Kelvin–Helmholtz roll-up. *J. Fluid Mech.* **243**, 183–226.

Ruelle, D. & Takens, F. 1971 On the nature of turbulence. *Commun. Math. Phys.* **20**, 167–169.

Salhi, A., Cambon, C. & Speziale, C. G. 1997 Linear stability analysis of plane quadratic flows in a rotating frame with applications to modelling. *Phys. Fluids* **9**, 2300–2309.

Schowalter, D. G., Van Atta, C. W. & Lasheras, J. C. 1994 A study of streamwise vortex structure in a stratified shear layer. *J. Fluid Mech.* **281**, 247–291.

Scinocca, J. F. 1995 The mixing of mass and momentum by Kelvin–Helmholtz billows. *J. Atmos. Sci.* **52**, 2509–2530.

Smyth, W. D., Klaassen, G. P. & Peltier, W. R. 1988 Finite amplitude Holmboe waves. *Geophys. Astrophys. Fluid Dyn.* **43**, 181–222.

Smyth, W. D. & Peltier, W. R. 1991 Instability and transition in finite amplitude Kelvin–Helmholtz and Holmboe waves. *J. Fluid Mech.* **228**, 387–415.

Smyth, W. D. & Peltier, W. R. 1994 Three-dimensionalization of barotropic vortices on the f-plane. *J. Fluid Mech.* **265**, 25–64.

Staquet, C. 1995 Two-dimensional secondary instabilities in a strongly stratified shear layer. *J. Fluid Mech.* **296**, 73–126.

Swinney, H. L. & Gollub, J. P. 1981 *Hydrodynamic Instabilities and the Transition to Turbulence.* Springer.

Thorpe, S. A. 1973 Experiments on instability and turbulence in stratified shear flow. *J. Fluid Mech.* **61**, 731–751.

Thorpe, S. A. 1985 Laboratory observations of secondary structures in Kelvin–Helmholtz billows and consequences for ocean mixing. *Geophys. Astrophys. Fluid Dyn.* **34**, 175–199.

Thorpe, S. A. 1987 Transitional phenomena and the development of turbulence in stratified fluids: A review. *J. Geophys. Res.* **92C**, 5231–5248.

Waleffe, F. 1990 On the three-dimensional instability of strained vortices. *Phys. Fluids* A **2**, 76–80.

Winant, C. D. & Browand, F. K. 1974 Vortex pairing: The mechanism of turbulent mixing layer growth at moderate Reynolds number. *J. Fluid Mech.* **63**, 237–255.

Winters, K. B., Lombard, P. N., Riley, J. J. & D'Asaro, E. A. 1995 Available potential energy and mixing in density-stratified fluids. *J. Fluid Mech.* **289**, 115–128.

Woods, J. D. 1968 Wave-induced shear instability in the summer thermocline. *J. Fluid Mech.* **32**, 791–800.